Inner structure of La Fossa di Vulcano (Vulcano Island, southern Tyrrhenian Sea, Italy) revealed by high-resolution electric resistivity tomography coupled with self-potential, temperature, and CO2 diffuse degassing measurements

A. Revil, Anthony Finizola, A. Piscitelli, E. Rizzo, T. Ricci, A. Crespy, B Angeletti, M. Balasco, Stéphanie Barde-Cabusson, L. Bennati, et al.

Inner structure of La Fossa di Vulcano (Vulcano Island, southern Tyrrhenian Sea, Italy) revealed by high-resolution electric resistivity tomography coupled with self-potential, temperature, and CO_2 diffuse degassing measurements

A. Revil,[1,2,3] A. Finizola,[4,5] S. Piscitelli,[6] E. Rizzo,[6] T. Ricci,[7] A. Crespy,[8] B. Angeletti,[8] M. Balasco,[6] S. Barde Cabusson,[9] L. Bennati,[9,10] A. Bolève,[3,11] S. Byrdina,[9,12] N. Carzaniga,[13] F. Di Gangi,[4] J. Morin,[5,14] A. Perrone,[6] M. Rossi,[12] E. Roulleau,[15] and B. Suski[16]

[1] La Fossa cone is an active stratovolcano located on Vulcano Island in the Aeolian Archipelago (southern Italy). Its activity is characterized by explosive phreatic and phreatomagmatic eruptions producing wet and dry pyroclastic surges, pumice fall deposits, and highly viscous lava flows. Nine 2-D electrical resistivity tomograms (ERTs; electrode spacing 20 m, with a depth of investigation >200 m) were obtained to image the edifice. In addition, we also measured the self-potential, the CO_2 flux from the soil, and the temperature along these profiles at the same locations. These data provide complementary information to interpret the ERT profiles. The ERT profiles allow us to identify the main structural boundaries (and their associated fluid circulations) defining the shallow architecture of the Fossa cone. The hydrothermal system is identified by very low values of the electrical resistivity (<20 Ω m). Its lateral extension is clearly limited by the crater boundaries, which are relatively resistive (>400 Ω m). Inside the crater it is possible to follow the plumbing system of the main fumarolic areas. On the flank of the edifice a thick layer of tuff is also marked by very low resistivity values (in the range 1–20 Ω m) because of its composition in clays and zeolites. The ashes and pyroclastic materials ejected during the nineteenth-century eruptions and partially covering the flank of the volcano correspond to relatively resistive materials (several hundreds to several thousands Ω m). We carried out laboratory measurements of the electrical resistivity and the streaming potential coupling coefficient of the main materials forming the volcanic edifice. A 2-D simulation of the groundwater flow is performed over the edifice using a commercial finite element code. Input parameters are the topography, the ERT cross section, and the value of the measured streaming current coupling coefficient. From this simulation we computed the self-potential field, and we found good agreement with the measured self-potential data by adjusting the boundary conditions for the flux of water. Inverse modeling shows that self-potential data can be used to determine the pattern of groundwater flow and potentially to assess water budget at the scale of the volcanic edifice.

[1]Department of Geophysics, Colorado School of Mines, Golden, Colorado, USA.
[2]Université Aix Marseille III, CNRS, Aix en Provence, France.
[3]UMR5559, Equipe Volean, University of Savoie, INSU, LGIT, CNRS, Bourget du Lac, France.
[4]Istituto Nazionale di Geofisica e Vulcanologia, Palermo, Italy.
[5]Now at Laboratoire GéoSciences Réunion, UMR7154, UR, IPGP, La Réunion, France.
[6]Laboratory of Geophysics, IMAA, CNR, Tito Scalo, Italy.
[7]INGV, Università Roma Tre, Rome, Italy.
[8]Université Aix Marseille III, CNRS, Aix en Provence, France.
[9]Laboratoire Magma et Volcan, Université Blaise Pascal, UMR6524, IRD, CNRS, Clermont-Ferrand, France.
[10]Now at Department of Earth and Atmospheric Sciences, Purdue University, West Lafayette, Indiana, USA.
[11]Also at Savoie Technolac, Sobesol, Le Bourget du Lac, France.
[12]IPGP, CNRS, Paris, France.
[13]Department of Geology and Geosciences, Università Milano-Bicocca, Milan, Italy.
[14]Panthéon-Sorbonne, Université Paris 1, Paris, France.
[15]GEOTOP-UQAM-McGill, Montreal, Quebec, Canada.
[16]Institut de Géophysique, Collège Propédeutique, Université de Lausanne, Lausanne, Switzerland.

1. Introduction

[2] Vulcano is a small volcanic island (3 × 7 km) located at the southernmost of the Aeolian Islands in the southern Tyrrhenian Sea in Italy (38°24′N, 14°58′E). This island was shaped during five main volcanic stages during the past 120,000 years. The two overlapping calderas of the island, the 2.5-km-wide Caldera del Piano on the southeast and the 3-km-wide Caldera della Fossa northwest of the island (Figure 1), were formed at about 98,000–77,000 and 24,000–13,000 years ago, respectively. Volcanism has migrated to the north of the island over time. La Fossa cone, which is the target of the present investigation, occupies the 3-km-wide Caldera della Fossa at the northwest end of the island. This edifice has been active throughout the Holocene and constitutes the location of most of the historical eruptions of Vulcano island. In the vicinity of the Fossa cone, the Vulcanello edifice forms a low, roughly circular peninsula, on the northern tip of Vulcano (Figure 1). This area was formed as an island beginning in 183 BC and was connected to the Vulcano island in 1550 AD during its last eruption. The latest eruption from Vulcano consisted of explosive activity from the Fossa cone from 1888 to 1890 [e.g., *Frazzetta et al.*, 1983, 1984].

[3] There are two main reasons why we choose to investigate La Fossa cone. The first reason is related to the geohazards associated with the activity of the active La Fossa cone. The population of the island increases to nearly 5,000 inhabitants during the summer from a few hundreds during the winter. The main geohazards at Vulcano are related to sin-eruptive pyroclastic surges, bombs and block fallout, phreatic explosions, gas hazard, debris flows, and landslides of altered flanks and the subsequent formation of tsunamis. The second reason is related to the relatively modest dimensions of this edifice and its strong hydrothermal activity. The Fossa cone is therefore a perfect natural laboratory to test the ability of geophysical methods to image the substructure of an active volcano. In addition, we are interested to see how geophysical signals can be used to monitor changes in its activity.

[4] The use of deep DC electrical resistivity tomography has recently gained in interest to map the substructure of volcanoes and active faults [e.g., *Storz et al.*, 2000; *Colella et al.*, 2004; *Diaferia et al.*, 2006; *Finizola et al.*, 2006; *Linde and Revil*, 2007a]. However, electrical resistivity tomography alone is notoriously difficult to interpret unequivocally. The main reason is that electrical resistivity of volcanic rocks depends on too much parameters including the water content, salinity, temperature, and cation exchange capacity of the porous material [e.g., *Waxman and Smits*, 1968; *Revil et al.*, 2002, and references therein]. Therefore, it is essential to add additional information to electrical resistivity tomograms to improve their interpretation in terms of geological and hydrogeological units [see *Revil et al.*, 2004b; *Finizola et al.*, 2006; *Coppo et al.*, 2008].

[5] Self-potential signals correspond to the passive measurement of the distribution of the electrical potential at the ground surface of Earth. Once filtered, these signals evidenced polarization mechanisms at depth. One of them is related to groundwater flow and is known as the streaming potential. *Gex* [1992] and *Di Fiore et al.* [2004] have performed self-potential measurements at the island of Vulcano. However, while these works were very useful, only specific parts of the volcano were covered by these investigations and self-potential signals were not interpreted quantitatively in terms of groundwater flow pattern.

[6] In this paper, we interpret a set of new high-resolution electrical resistivity tomograms crossing the Fossa cone of Vulcano Island. By high resolution, we mean that the spacing between the electrodes is only of 20 m. This allows a resolution that is much higher than electromagnetic methods (e.g., TDEM) and classical large-scale resistivity surveys without the use of a long cable (>1 km). To help the interpretation of these tomograms, additional measurements of temperature, self-potential, and CO_2 flux from the soil were carried out along the resistivity profiles at the same locations than the electrodes used for the resistivity surveys. The temperature and CO_2 flux reveal the position of the permeable flow pathways of the hydrothermal system. We show that forward and inverse modeling of the self-potential data allow constraining the pattern of groundwater flow. All these measurements result in a unique data set, at a kilometer scale, over an active volcano. This data set reveals for the first time the inner substructure of La Fossa cone stratovolcano, showing the main geological structure and the extent of the hydrothermal system inside the edifice.

2. Geological Background

[7] Vulcano Island represents the southernmost portion of a NW-SE elongated volcanic ridge that comprises seven islands forming the Aeolian Archipelago (southern Italy). This archipelago is related to the subduction of the African plate underneath the European Plate [*Keller*, 1980; *Ellam et al.*, 1989]. The ridge is affected by a regional, NW-SE to N-S striking fault system [*Gasparini et al.*, 1982]. In ancient times, the Romans believed that Vulcano was the chimney to the forge of the god Vulcan. The glow of eruptions was thought to be from his forges and the island had grown because of his periodic clearing of cinders and ashes. The earthquakes that either preceded or accompanied the explosions of ashes were considered to be due to Vulcan himself making weapons for the other gods.

[8] Nowadays, we know that the island has been shaped during five distinct stages. These stages are Vulcano Primordiale, Piano Caldera, Lentia Complex, La Fossa Caldera, and Vulcanello. The history of Vulcano begins with the formation of a stratovolcano. The collapse of this stratovolcano produces the Piano caldera (see CP in Figure 1 and *Santacroce et al.* [2003]). Then, this caldera was partially filled with pyroclastic deposits and lava flows. The stratovolcano and its caldera form the southern part of the island

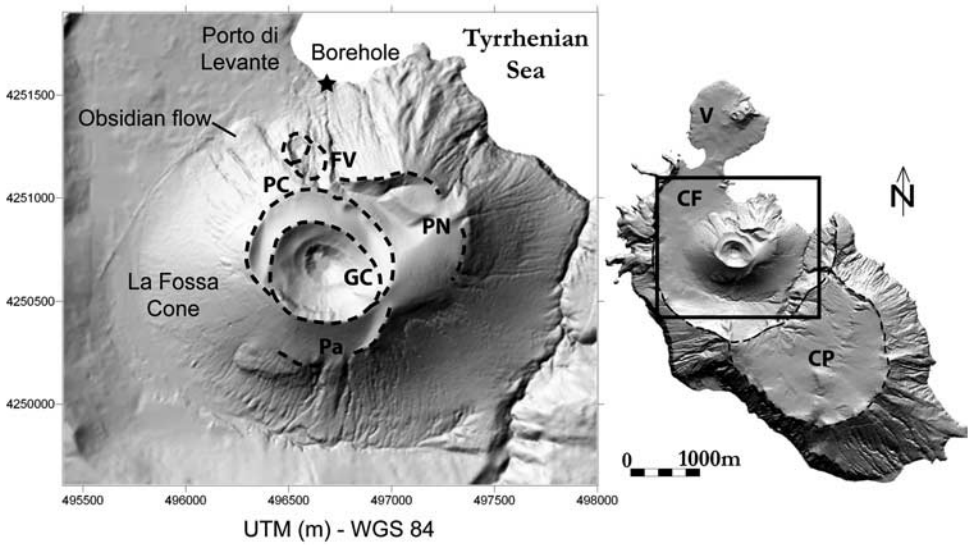

Figure 1. Map of the Island of Vulcano (Italy). Abbreviations are as follows: PN, Punte Nere; Pa, Palizzi; FV, Forgia Vecchia; PC, Pietre Cotte; GC, Gran Cratere; V, Vulcanello, CF, Caldera della Fossa; and CP, Caldera del Piano.

of Vulcano. The Fossa cone grew within the Fossa caldera, which constitutes the northern part of the island (Figure 1).

[9] The Fossa cone is a small stratovolcano with an altitude of 391 m a.s.l. (meters above sea level; see Figures 2 and 3). The diameter of its base is about 2 kilometers. The Fossa cone began to form 6,000 years ago [*Dellino and La Volpe*, 1997; *De Rosa et al.*, 2004]. Six volcanic successions: Punte Nere, Palizzi, Caruggi, Forgia Vecchia, Pietre Cotte and Gran Cratere (post-1739), with different vent locations and eruptive histories, shaped the edifice [*Dellino and La Volpe*, 1997; *De Rosa et al.*, 2004, *De Astis et al.*, 2007]. Each succession follows the same evolution starting with pyroclastic surges and ending with the emission of highly viscous lava flows. All the explosive and effusive products of La Fossa cone have high potassium contents and a chemical composition ranging from trachytic to the more evolved rhyolitic composition [*Keller*, 1980].

[10] The last eruption of the Fossa cone occurred from 1888 to 1890. In the same century, Vulcano produced three eruptions lasting more than one month (1822–1823, 1873, and 1886). The violence of the last eruption (1888–1890) was marked by the fall of volcanic bombs and blocks, about ~1 m in diameter, at ~1 km from the vent. Breadcrust bombs, distinctive of this style of eruption, were ejected about 500 m. These bombs are characterized by an aphyric glassy matrix of rhyolitic composition and xenoliths of trachytic composition [*De Fino et al.*, 1991]. Explosions were intermittent and separated by quiet periods lasting a few minutes to a few days. Explosions varied in strength. Only the largest explosions, separated by longer quiet periods, could throw blocks and bombs. No domes or lava flows were produced at the end of this eruption.

[11] Nowadays, the peculiarity of La Fossa volcano is the occurrence of thermal and seismic crisis. The last one occurred in 2004–2006 [*Granieri et al.*, 2006; *Aubert et al.*, 2008] and was characterized by strong increases of the temperature of the fumaroles and an increase of the surface area covered by the fumarolic field (see below). Chemical changes in the fumaroles and the occurrence of shallow seismic activity were indicative of an increase of the input of magmatic fluids [*Granieri et al.*, 2006]. However, during such episodes, there was no evidence of magmatic rising.

[12] There are three types of upper formations of the Fossa cone: (1) The former is constituted of the Palizzi pumice deposit, mainly scattered along the southern slope of La Fossa cone and with a maximum thickness of 2 m at the break in slope of the volcano [*Frazzetta et al.*, 1983]. The pumice fragments range in size from several centimeters to about 30 cm, with a mean value of about 10 cm. The glass matrix of the fragments has a trachytic composition. (2) The latter constituting the substratum is formed by a very impermeable fine-grained hydromagmatic tuff (Figure 2) and (3) the grey ashes from Gran Cratere that were deposited all over the edifice during the 1888–1890 eruption.

3. Field Investigations

[13] In October 2005, May 2006, and October 2006, we performed three geophysical surveys (electrical resistivity, self-potential, temperature, and soil CO_2 flux) that were organized along nine profiles crossing the entire Fossa cone. The position of these profiles is shown on Figure 2. Note that because we know nothing about the temporal variation of these, we did not try to provide a 3-D reconstruction of these data in the present work. We present in this section the methodology employed for the various measurements

3.1. Electrical Resistivity Profiles

[14] Because of their sensitivity to porosity, water saturation, and the presence of clays and zeolites minerals, DC-electrical resistivity and electromagnetic methods (e.g., time domain electromagnetics) are efficient tools to image active volcanoes [*Fitterman et al.*, 1988; *Zohdy and Bisdorf*, 1990; *Lénat et al.*, 2000]. DC-electrical resistivity measurements were obtained along the nine profiles displayed in Figure 2.

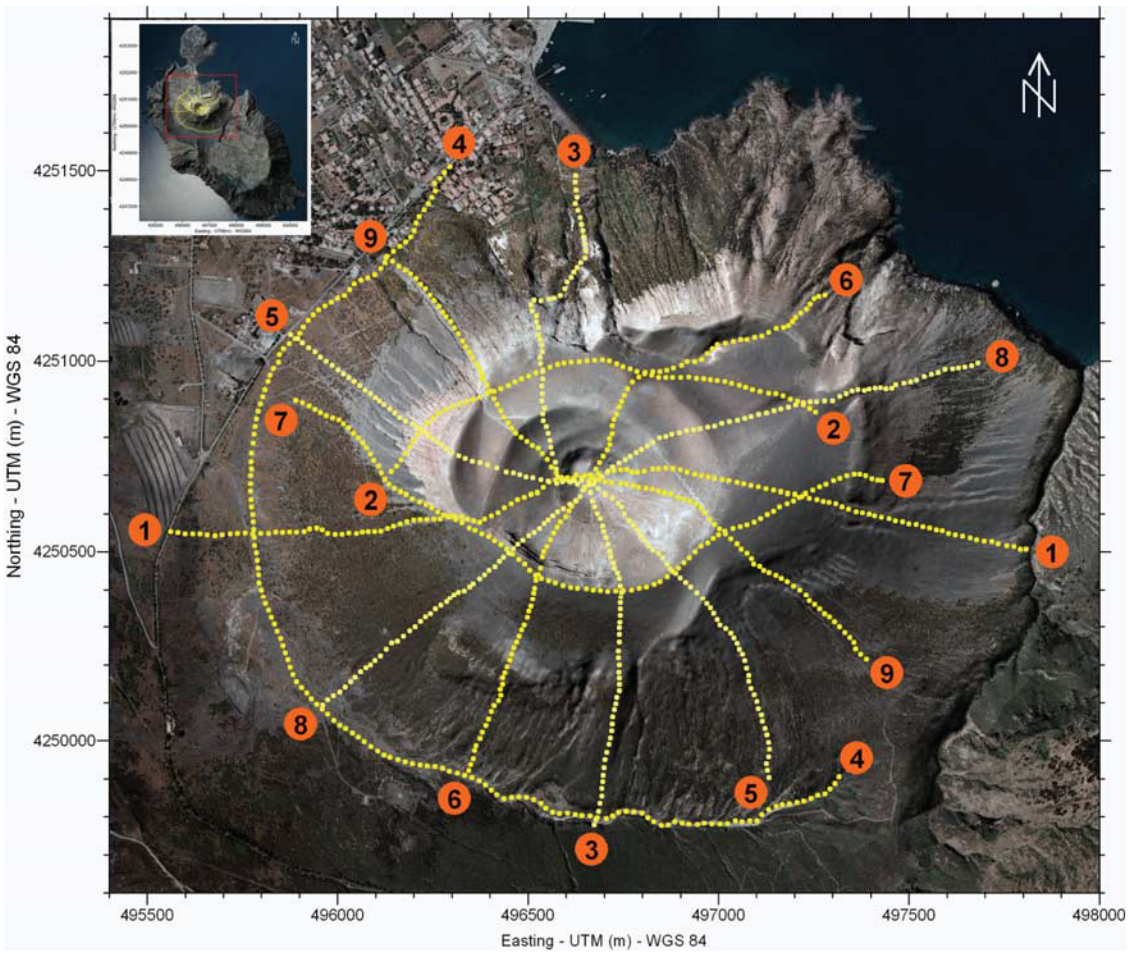

Figure 2. Position of the investigated area on the Fossa cone. Nine profiles (labeled from 1 to 9) have been performed crossing the Fossa edifice. The bright areas on the flanks of the volcano correspond to the hydromagmatic tuff discussed in the main text.

The measurements were performed using a set of 64 brass electrodes with a spacing of 20 m. We use a shielded cable of 1.26 km made of 8 segments of 160 m each. Two or three roll-alongs of the electrodes were performed to complete each profile. Contact between the electrodes and the ground was improved by adding salty water at the base of each electrode to decrease the contact resistance between the ground and the electrodes. We used the Wenner array for its good signal-to-noise ratio. Reciprocity measurements (performed on one profile) show an uncertainty smaller than 7%. Dipole-dipole measurements provide complementary information with respect to the Wenner array. However, we did not perform such measurements because of time constraints.

[15] The resistivity data were inverted with RES2DINV [*Loke and Barker*, 1996], which uses the smoothness-

Figure 3. The Fossa cone observed from the south.

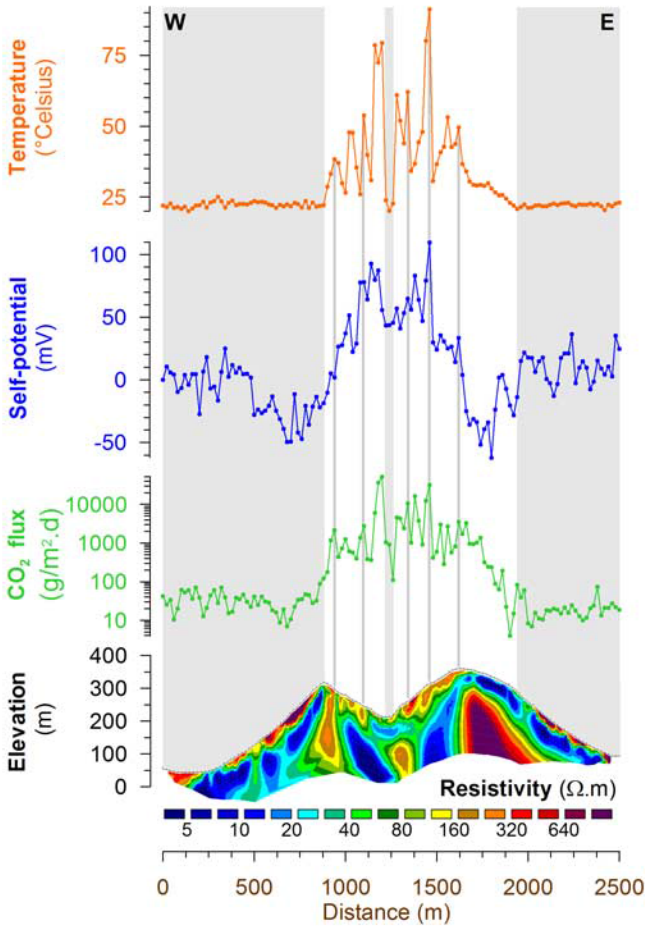

Figure 4. Temperature, self-potential, soil CO_2 flux, and electrical resistivity tomogram along profile 1. These data show that the main activity is constrained inside the crater, which is characterized by self-potential, CO_2, and temperature anomalies. Note that the ground surface of the central part of the crater is cold.

constrained method [*Constable et al.*, 1987] to perform the inverse problem:

$$(\mathbf{J}^T\mathbf{J} + \alpha\mathbf{F})\mathbf{d} = \mathbf{J}^T\mathbf{g} - \alpha\mathbf{F}\mathbf{r}, \quad (1)$$

where $\mathbf{F}$ is a smoothing matrix, $\mathbf{J}$ is the Jacobian matrix of partial derivatives, $\mathbf{r}$ is a vector containing the logarithm of the model resistivity values, α is the damping factor, $\mathbf{d}$ is the model perturbation vector, and $\mathbf{g}$ is the discrepancy vector. The discrepancy vector, $\mathbf{g}$, contains the difference between the calculated and measured apparent resistivity values. The magnitude of this vector is given by a RMS (root-mean squared) value. The algorithm seeks to reduce this quantity in an attempt to find a better model after each iteration. The model perturbation vector, $\mathbf{d}$, is the change in the model resistivity values calculated using the above equation which normally results in an "improved" model. The uniqueness of the solution of the inverse problem is an issue here [see, e.g., *Linde and Revil*, 2007a]. This means that for the same data set, there are several possible resistivity models that fit the data equally well [e.g., *Auken and Christiansen*, 2004; *Binley and Kemna*, 2005]. Additional information can be helpful to stabilize the inversion process. Starting from an initial model, RES2DINV looks for an improved model with calculated apparent resistivity values closer to the measured values. We used various initial models to test the stability of the inversion process. Starting the iterations with either a uniform resistivity model or the apparent resistivity pseudosection did not alter the final result.

[16] Topography was also included in the inversion process. Topography was extracted from a very precise digital elevation map (DEM of 1 × 1 m) of La Fossa cone provided by Maria Marsella (see also *Baldi et al.* [2002]). North and east UTM coordinates were obtained from a portable GPS receiver. Four electrical resistivity tomograms are displayed in Figures 4–7. Accounting for the complex geometry of the volcano, a 3-D inversion of ERT would be necessary to define the complex structural heterogeneities of the Fossa edifice. However, we show below that 2-D inversion of ERT provides an image that is consistent with

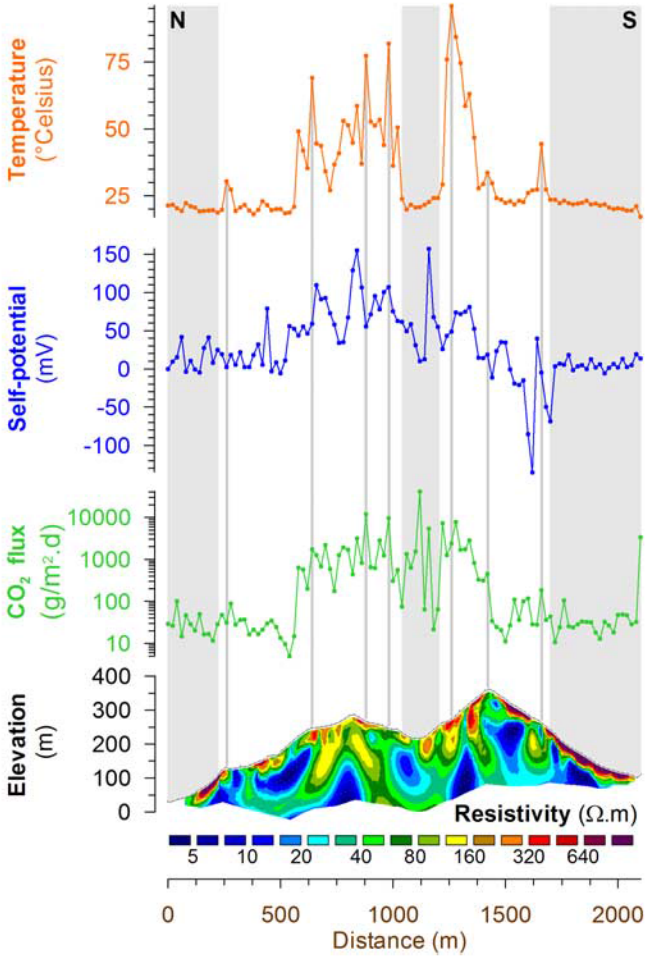

Figure 5. Temperature, self-potential, soil CO_2 flux, and electrical resistivity tomogram along profile 3. Note that the bottom part of the crater is cold. On the northern flank of the edifice (the left side of the figure), a conductive area is laterally limited by two thermal anomalies. These anomalies represent the boundary of the Forgia Vecchia crater which last eruption occurred in 1727.

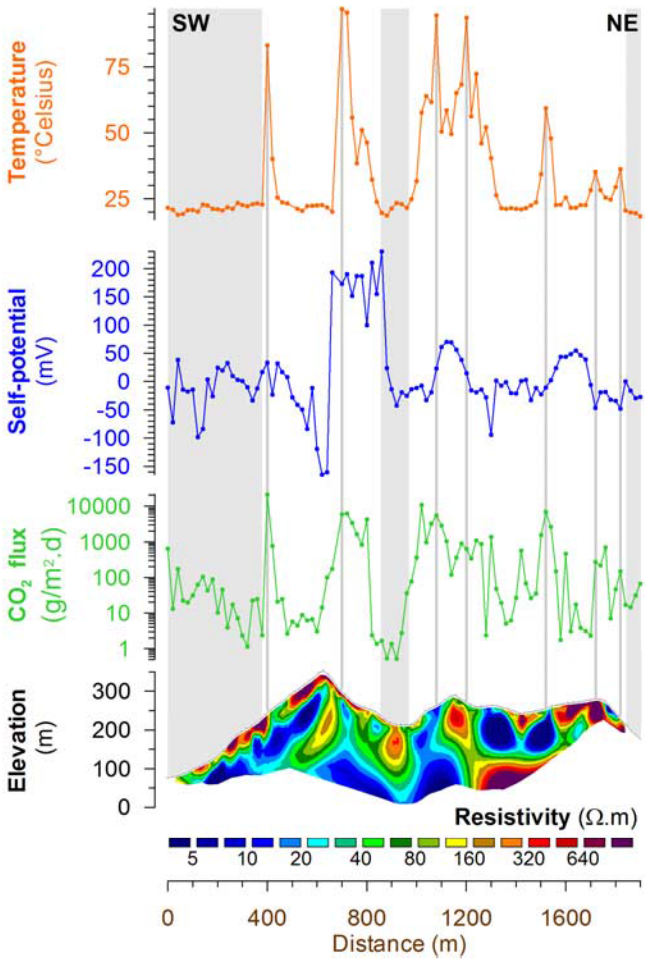

Figure 6. Temperature, self-potential, soil CO_2 flux, and electrical resistivity tomogram along profile 6. Note the M-shape of the temperature, self-potential, and CO_2 anomalies inside the crater.

the other data (self-potential, temperature, and CO_2 flux) in order to define the architecture of the volcano.

3.2. Temperature

[17] Thermal probes and a digital thermometer were used to measure the temperature of the ground. Each temperature measurement was done in four steps. First, we hammered a steel rod (2 cm in diameter) into the ground to a depth of 30 ± 2 cm. Second, a thermal probe was inserted into the hole at the precise depth of 30 ± 1 cm by means of a graduated wooden stick. Third, the hole around the stick was filled and compacted. Fourth, after 10 to 15 min (this duration is required to achieve thermal equilibrium), a temperature reading is performed [see *Finizola et al.*, 2002, 2003]. The duration to reach thermal equilibrium was checked by looking at the time variation of the temperature. We observed that the temperature stabilized in less than 10 min.

[18] The temperature profile provides an independent way to see the extension of the hydrothermal body in the vicinity of the ground surface. The temperature was measured with a sensitivity of 0.2°C. Owing to the maximum amplitude of diurnal variation at Vulcano at 30 cm depth during the summer season (1.2°C), and owing to the maximum amplitude of seasonal variation, from 12.2 to 27.2°C respectively in January and August [*Lo Cascio and Navarra*, 1997], a temperature above 30°C can be considered as indicative of the underground geothermal system. A map of the interpolated temperature is shown on Figure 8.

[19] It is important to note that our CO_2 flux, self-potential, and temperature measurements were obtained at different periods during the last 2004–2006 crisis, which began in November 2004 [*Granieri et al.*, 2006]. However, the amplitude the anomalies are not of primary importance because we will only use temperature anomalies as a way to detect qualitatively preferential fluid flow pathways in the hydrothermal system.

3.3. CO_2 Diffuse Degassing

[20] The CO_2 diffuse degassing measurements were obtained with a spacing of 20 m (uncertainty <5%). The methodology is described in details in the work of *Chiodini et al.* [1996, 1998]. The accumulation chamber method allows to measure quickly the CO_2 fluxes from the soil in a wide interval from 0.2 to several hundreds g m^{-2} day^{-1}. This method does not require corrections or assumptions on the characteristics of the soil. The instrumentation consists in an IR spectrometer, to measure CO_2 fluxes from 0 to

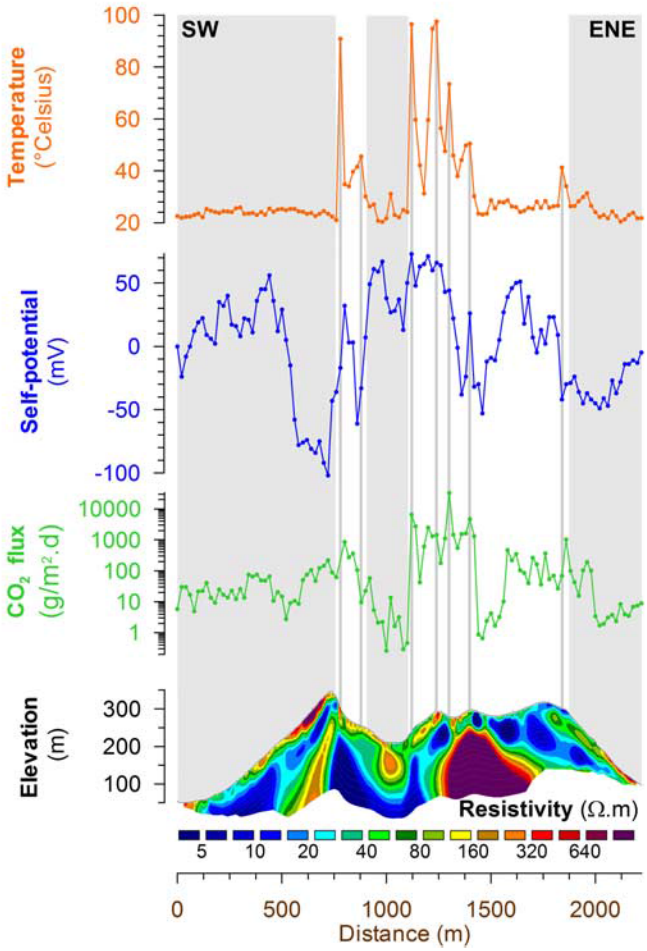

Figure 7. Temperature, self-potential, soil CO_2 flux, and electrical resistivity tomogram along profile 8.

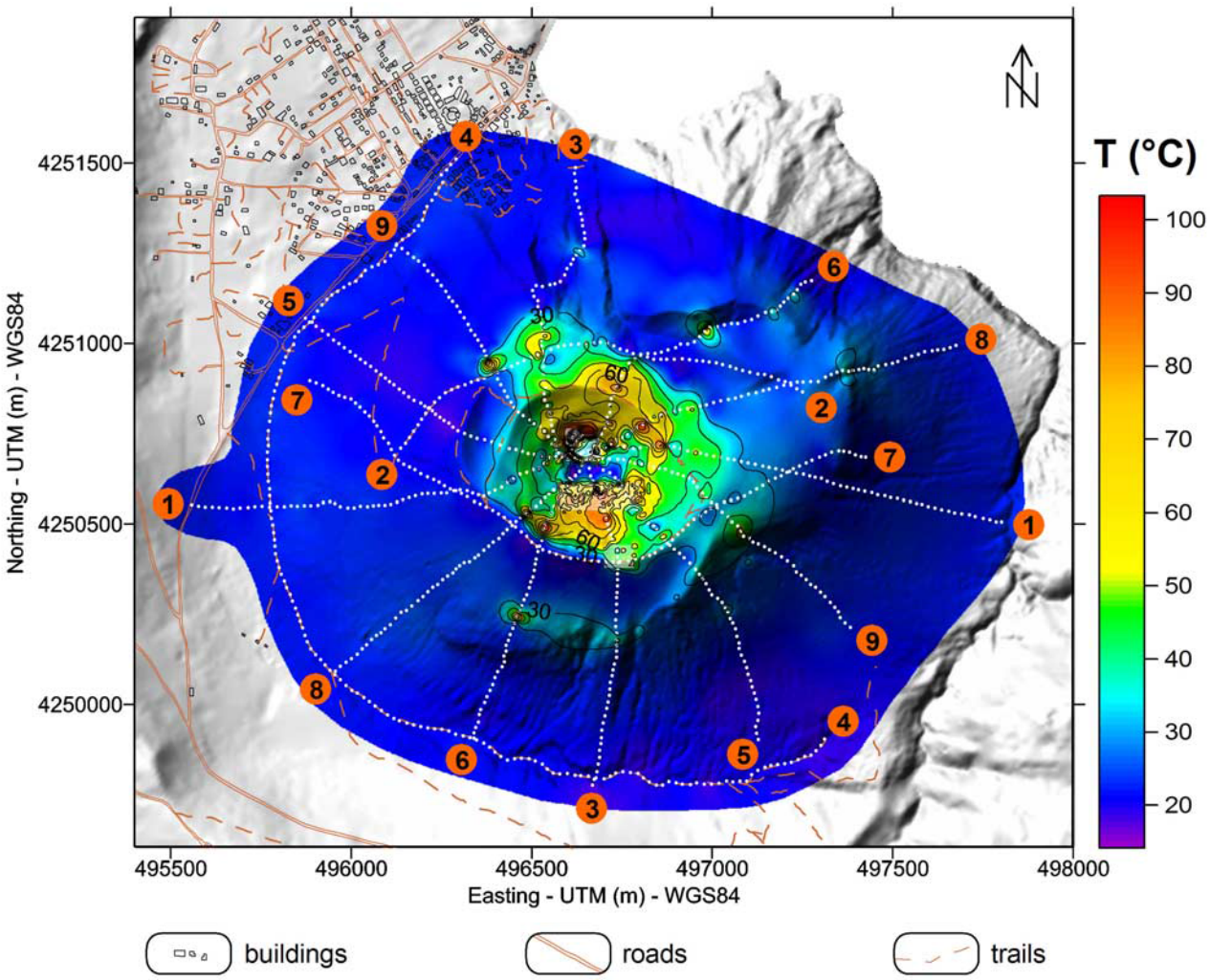

Figure 8. Map of the temperature at a depth of 30 cm superimposed on the DEM of La Fossa cone. The white dots correspond to the location of the temperature measurements of the present study. The dots inside the La Fossa crater correspond to the detailed temperature survey (at the same depth of 30 cm) reported by *Aubert et al.* [2008]. Note that the bottom of the crater is cold (<30°C). Thermal anomalies are sometimes observed on the flanks of the volcano. In this case these anomalies are indicative of the boundaries of ancient craters.

2000 μmol/mol (2% vol.), an accumulation chamber (type A: dead volume 30 cm^3), and a PDA to plot the CO_2 concentration increase. The accumulation chamber is stood on the ground so that the atmospheric air cannot penetrate inside. The gas permeating from the soil accumulates in the dead volume, thus the CO_2 concentration increases; every second the gas is analyzed by the IR spectrometer and re-injected in the accumulation chamber so as not to deplete the CO_2 concentration. The PDA software displays a curve representing the variation of the concentration of CO_2 versus time. This rate is directly proportional to the flux of CO_2 from the soil, expressed in g m^{-2} day^{-1} (the constant of proportionality depends on the instrument dead volume and on the atmospheric pressure).

[21] Carbon dioxide anomalies have their origin in magma degassing inside the volcanic system. The gas follows the same preferential pathways as the hydrothermal fluids, providing information about the permeability distribution of the edifice; high fluxes suggest permeable pathways from the hydrothermal system to the ground surface owing to the presence of fractures.

[22] A recent study by *Granieri et al.* [2006] shows that in quiet periods, La Fossa crater area releases diffusively about 200 ton day-1 of CO_2 from a surface of 0.5 km^2 while during crises the CO_2 output may increase of one order of magnitude. These data suggest that a significant volume of degassing magma exists at depth and that during crises the increasing of CO_2 diffuse degassing is due to the opening of new fractures at shallow levels and the consequent increasing of the permeability of the soil. This could be due to the shallow seismicity or to a generalized increase of the pore pressure in the volcanic system.

3.4. Self-Potential

[23] The self-potential (SP) method measures the distribution of the electric potential at the surface of Earth (and or

in boreholes) with respect to a reference electrode [e.g., *Corwin and Hoover*, 1979; *Lénat*, 2007]. Sources of self-potential fields include large-scale Earth currents due to ionospheric activity, chemical potential gradients [*Maineult et al.*, 2005, 2006], redox potentials [*Linde and Revil*, 2007a], and electrokinetic conversion associated with fluid movement through porous materials (the so-called streaming potential). In active volcanoes, the main source of self-potential anomalies is related to the flow of the groundwater [*Massenet and Pham*, 1985; *Ishido et al.*, 1997; *Bedrosian et al.*, 2007]. Self-potential is the only method that is directly sensitive to the pattern of groundwater flow and to changes in the seepage velocity [see *Perrier et al.*, 1998; *Kulessa et al.*, 2003a, 2003b; *Rizzo et al.*, 2004; *Suski et al.*, 2004, 2006; *Hase et al.*, 2005; *Titov et al.*, 2005; *Jardani et al.*, 2006b, 2007; *Wishart et al.*, 2006].

[24] To perform the self-potential measurements, we used a pair of nonpolarizing $Cu/CuSO_4$ electrodes. The microporous nature of the end-contacts of these electrodes (made of a low-permeability wood) avoids leakage of the $CuSO_4$ solution during contact between with the ground. Wood is also much more durable than the ceramics that is more commonly used to make commercial electrodes. The difference of electrical potential between the reference electrode (arbitrarily placed at the beginning of the profile) and the moving electrode was measured with a calibrated high impedance voltmeter (METRIX MX20, sensitivity of 0.1 mV, input impedance of $\sim$100 MΩ). When interpreting self-potential data, we have to consider that the value of the self-potential itself is meaningless. Only the gradient of the self-potential data (that is the electrical field) has a physical meaning.

[25] Before and after each series of measurements, the reference electrode and the roving electrode were put face-to-face to check that the difference of potential between the two electrodes was less than 2 mV (if this is not the case, the static value is removed to all the measurements). At each station, a small hole ($\sim$10 cm deep) was dug to improve the electrical contact between the electrode and the ground. For each self-potential measurement, the value of the electrical resistance was also measured prior the self-potential measurement. Most of the time, the moisture in the soil was sufficiently high to insure low enough impedance contact between the scanning electrode and the ground. However, if the contact resistance was high (>1 MΩ), a small amount of a saturated $CuSO_4$ solution was placed at the bottom of the hole to decrease the contact resistance between the electrode and the ground. We did not observe the type of drift reported by *Corwin and Hoover* [1979] associated with watering the electrodes. The standard deviation on the measurements is determined by performing twenty measurements few meters around the same station. At Vulcano, it is on the order of 12 mV in average. This relatively large standard deviation is mainly due to the strong heterogeneity of the resistivity distribution near the surface of the ground. In the following, we will consider that the self-potential measurement is a random process described by a Gaussian distribution (as shown by *Linde et al.* [2007]) with a standard deviation of 12 mV.

[26] To perform the self-potential measurements, a long wire was used to connect the two electrodes to a Metrix MX20 voltmeter. The distance between two successive measurement stations was 20 m. The total length of the wire was 400 m, and consequently, 20 measurements were realized with the same reference. The advantage of this procedure was to avoid cumulative errors by changing the reference too often along the same profile. Every 400 m, a new reference station was established. As the profiles were several kilometers long, several base stations were used to cover a profile. After the survey, the entire self-potential profile was reconstructed using the first reference station as the unique reference for the entire profile.

4. Laboratory Measurements

[27] In this section, we report laboratory measurements of the electrical conductivity and streaming potential of a collection of 21 core samples from the edifices of La Fossa di Vulcano and Stromboli (a nearby volcano that is strongly active). Electrical conductivity measurements were performed on each sample in the frequency range from 20 Hz to 100 kHz, at room temperature (20 $\pm$ 2°C), using NaCl solutions with the following pore fluid conductivities σ_f = 0.1 S m^{-1} and 0.5 S m^{-1}(pH 7). The conductivity of the pore water sampled at the base of the volcano, in different wells, is in the range 0.1 to 2.8 S m^{-1} and the pH is in the range 5.4 to 7.9 with a mean equal to 6.7 [*Cortecci et al.*, 2001]. We believe that a water conductivity of 0.1 S m^{-1} is representative of fresh (meteoric) waters while high conductivities are indicative of a mixture of fresh water and seawater and possibly hydrothermal fluids. The water flowing along the slopes is locally affected by fumarolic fields is also enriched with the fumarolic acid condensates coming from the pericrateric high-temperature fumaroles along the fluid flow pathways highlighted by the resistivity tomograms and temperature anomalies.

[28] We use a Waynekerr-6425 impedance meter for the resistivity measurements. The samples were placed between two stainless steel electrodes. Two circular pieces of brine-saturated filter paper were used to ensure good electrical contacts between the sample and the electrodes. The jacketed samples were first washed with demineralized water and dried at 60°C for 2 days. The jacket was made of a hydrophobic adhesive. The samples were held under vacuum prior to be saturated with a degassed brine at 0.1 S m^{-1} (see *Revil et al.* [2002] for a detailed version of the procedure). Following the initial measurements, the salinity of the brine was then changed by placing the samples in a 0.5 S m^{-1} electrolyte and by letting the brine diffuses to the sample through the two end-faces for 1 week (see *Revil* [1995] for tests of the effectiveness of this procedure). The results are reported in Table 1.

[29] Electrical conductivity is sensitive to the water content, the mineralization of the pore water (salinity), the cation exchange capacity of the clay minerals (surface conductivity), and temperature [see *Waxman and Smits*, 1968; *Revil et al.*, 1998, 2002; *Kalscheuer et al.*, 2007; *Niwas et al.*, 2007; *Jin et al.*, 2007; *Tabbagh and Cosenza*, 2007; *Shevnin et al.*, 2007]. In this paper, we assume a simple linear conductivity model,

$$\sigma = \frac{1}{F}\left[\sigma_f + (F-1)\sigma_s\right], \tag{2}$$

Table 1. Measurements of Electrical Resistivity and Streaming Potential Coupling Coefficient of Various Samples From Stromboli and La Fossa di Vulcano[a]

Samples	Resistivity, $\sigma_f = 0.1$ S m^{-1} (Ω m)	C, $\sigma_f = 0.1$ S m^{-1} (mV m^{-1})	Resistivity, $\sigma_f = 0.5$ S m^{-1} (Ω m)	C, $\sigma_f = 0.5$ S m^{-1} (mV m^{-1})
S-B1	698	−3.9	167	−1.79
S-B2	638	−2.6	192	−0.54
S-B3	707	−4.1	222	−0.75
S-LF1	802	−5.2	180	−0.90
S-LF2	728	−4.1	179	−1.71
S-LF3	421	-	53	-
S-LF4	575	−2.1	205	−0.61
S-LF5	327	−2.0	113	−1.47
S-LF6	1040	−2.4	160	−1.05
S-T1	656	−2.0	125	−0.87
S-T2	452	−2.9	102	−0.89
S-T3	626	−5.1	135	−0.62
S-T4	713	−3.4	130	−0.80
V-LF1	378	−5.4	74	−2.22
V-LF2	265	−4.2	63	−1.09
V-LF3	345	−3.4	57	−0.92
V-Lb1	227	−4.3	61	−0.91
V-Lb2	306	−2.8	55	−0.96
V-Lb3	712	−3.8	94	−0.77
V-Lb4	315	−2.5	40	−1.31
V-T1	22	−3.4	7.8	−0.12

[a]Abbreviations are as follows: S-B, Vancori Basalt (Stromboli); S-LF, Lava Flow (Piscità, Stromboli); S-T, Tuff (Pizzo, Stromboli); V-LF, Lava flow (Vulcano); V-Lb, Lava Flow (borehole; see position in Figure 1); and V-T, Tuff (Vulcano). The uncertainties associated with the measurements of the resistivity and the coupling coefficient are ~5% (determined from the reproducility of the measurements).

which can be considered as a first-order approximation of the nonlinear models proposed by *Revil et al.* [1998, 2002]. In equation (2), F is the electrical formation factor (a power law function of porosity widely known as Archie's law) and σ_s is the surface conductivity occurring mainly in the Stern layer at the water-mineral interface [*Revil and Glover*, 1998]. Surface conductivity usually results from the cation exchange capacity of clay minerals and zeolites and is indicative of the alteration of the rock [see *Roberts and Lin*, 1997; *Revil et al.*, 2002; *Bernard et al.*, 2007]. An electrochemical model of surface conductivity has been developed recently by *Leroy and Revil* [2004] that can be used to determine the effect of the composition of the pore fluid and mineralogy upon the surface conductivity of the material. Using equation (2) and the resistivity data reported in Table 1, we determined the value of the formation factor and surface conductivity and their uncertainties. These values are reported in Table 2. We note that the tuff of Vulcano is characterized by a very high surface conductivity, which explains the very low electrical resistivity observed by the resistivity surveys for this formation (see Figures 4–7).

[30] We also performed measurements of the streaming potential coupling coefficient C at room temperature (20 ± 2°C) for 21 rock samples. The streaming potential coupling coefficient is the key-material property required to compute the self-potential contribution associated with groundwater flow (see section 5 below) [e.g., *Tosha et al.*, 2003]. The experimental setup for the measurement of the streaming potential coupling coefficient is shown Figure 9a. A given hydraulic head is imposed on the cylindrical sample placed at the bottom of the tube by adding water to the water column in the tube in such a way that the hydraulic head is maintained constant above the rock sample. The gradient of the fluid pressure is controlled by the hydraulic head in the tube (imposed by the head of a much more important reservoir in contact with it) and the length of the sample. The electrical potential resulting from the flow of the pore water is measured with two nonpolarizable $Ag/AgCl_2$ electrodes (Ref321/XR300, Radiometer Analytical) located in the vicinity of the end-faces of the sample (Figure 9a).

Table 2. Formation Factor and Surface Conductivity Determined From Electrical Conductivity Measurements[a]

Samples	F	σ_S(10^{-4} S m^{-1})	Porosity
S-B1	90 ± 4	4.3 ± 1	0.15
S-B2	112 ± 6	7.6 ± 2	0.09
S-B3	132 ± 7	7.3 ± 2	0.13
S-LF1	95 ± 4	2.9 ± 1	0.12
S-LF2	97 ± 4	4.4 ± 2	0.13
S-LF3	28 ± 2	9.2 ± 2	0.18
S-LF4	130 ± 8	10.5 ± 3	0.12
S-LF5	71 ± 3	18.1 ± 3	0.12
S-LF6	82 ± 3	1.55 ± 0.20	0.10
S-T1	63 ± 3	0.7 ± 0.3	0.12
S-T2	54 ± 2	5.3 ± 1.0	0.12
S-T3	71 ± 4	3.3 ± 1.0	0.10
S-T4	65 ± 4	0.1 ± 0.1	0.10
V-LF1	38 ± 3	2.8 ± 0.1	0.44
V-LF2	34 ± 2	11.4 ± 2.4	0.48
V-LF3	29 ± 2	3.0 ± 0.4	0.48
V-Lb1	34 ± 4	18.3 ± 2.5	0.14
V-Lb2	28 ± 2	0.4 ± 0.1	0.14
V-Lb3	49 ± 4	4.5 ± 1.0	0.13
V-Lb4	21 ± 1	12.6 ± 2	0.14
V-T1	4.8 ± 1	310 ± 20	-

[a]Abbreviations are as follows: S-B, Vancori Basalt (Stromboli); S-LF, Lava Flow (Piscità, Stromboli); S-T, Tuff (Pizzo, Stromboli); V-LF, Lava flow (Vulcano); V-Lb, Lava Flow (borehole; see position in Figure 1); and V-T, Tuff (Vulcano).

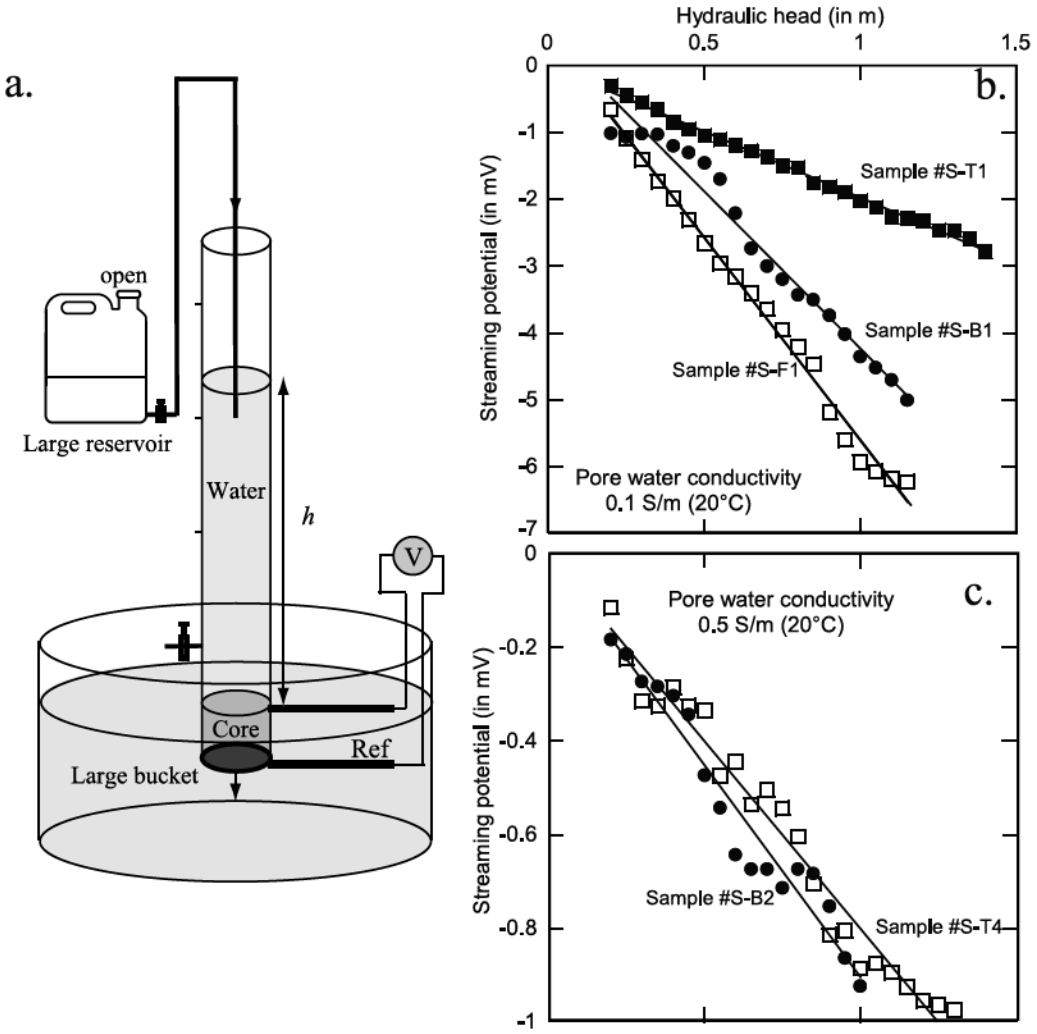

Figure 9. Examples of typical runs for five different volcanic rock samples. (a) Sketch of the experimental setup used to measure the streaming potential coupling coefficient. The jacketed sample is placed at the bottom of a Plexiglas tube. The record of the self-potentials during the flow of the electrolyte through the sample is done with Ag/AgCl electrodes ("Ref" is the reference electrode). The hydraulic heads are maintained constant at different levels with the help of the large reservoir and the valve. The electromotive force is recorded at these levels between the end-faces of the core sample with a high-impedance voltmeter. (b) Streaming potentials versus hydraulic heads using a solution at 0.1 S m^{-1} (this value is typical of the conductivity of the pore water flowing in the shallow aquifers of Vulcano). (c) Same with a solution at 0.5 S m^{-1}. In both cases we observe linear relationships. The streaming potential coupling coefficient is equal to the slope of these linear trends. The denomination of the samples is the same as in Tables 1 and 2.

The difference of the electrical potential measured between the end-faces of the porous pack divided by the length of the sample is the streaming electrical field associated with the flow of the brine through the sample. The voltages are measured with a Metrix MX-20 voltmeter (internal impedance 100 MΩ, sensitivity 0.1 mV).

[31] In the viscous-laminar flow regime (characterized by low Reynolds numbers; see *Bolève et al.* [2007a]), the difference of the electrical potential measured in the vicinity of the end-faces of the porous medium is proportional to the imposed hydraulic head H (Figures 10b and 10c) (this trend is nonlinear in the inertial-laminar flow regime). The slope of the linear trend of streaming potential versus head is the streaming potential coupling coefficient [e.g., *Revil et al.*, 2004a; *Bolève et al.*, 2007a, 2007b],

$$C = \left(\frac{\partial \varphi}{\partial H}\right)_{j=0}. \tag{3}$$

The values of the streaming potential coupling coefficient for the different samples are reported in Table 1.

[32] After completion of the electrical conductivity and streaming potential measurements, we determined the porosity and matrix density from classical triple weight measurements. The samples were first washed with demineralized water for 1 week to let the salt diffusing out from

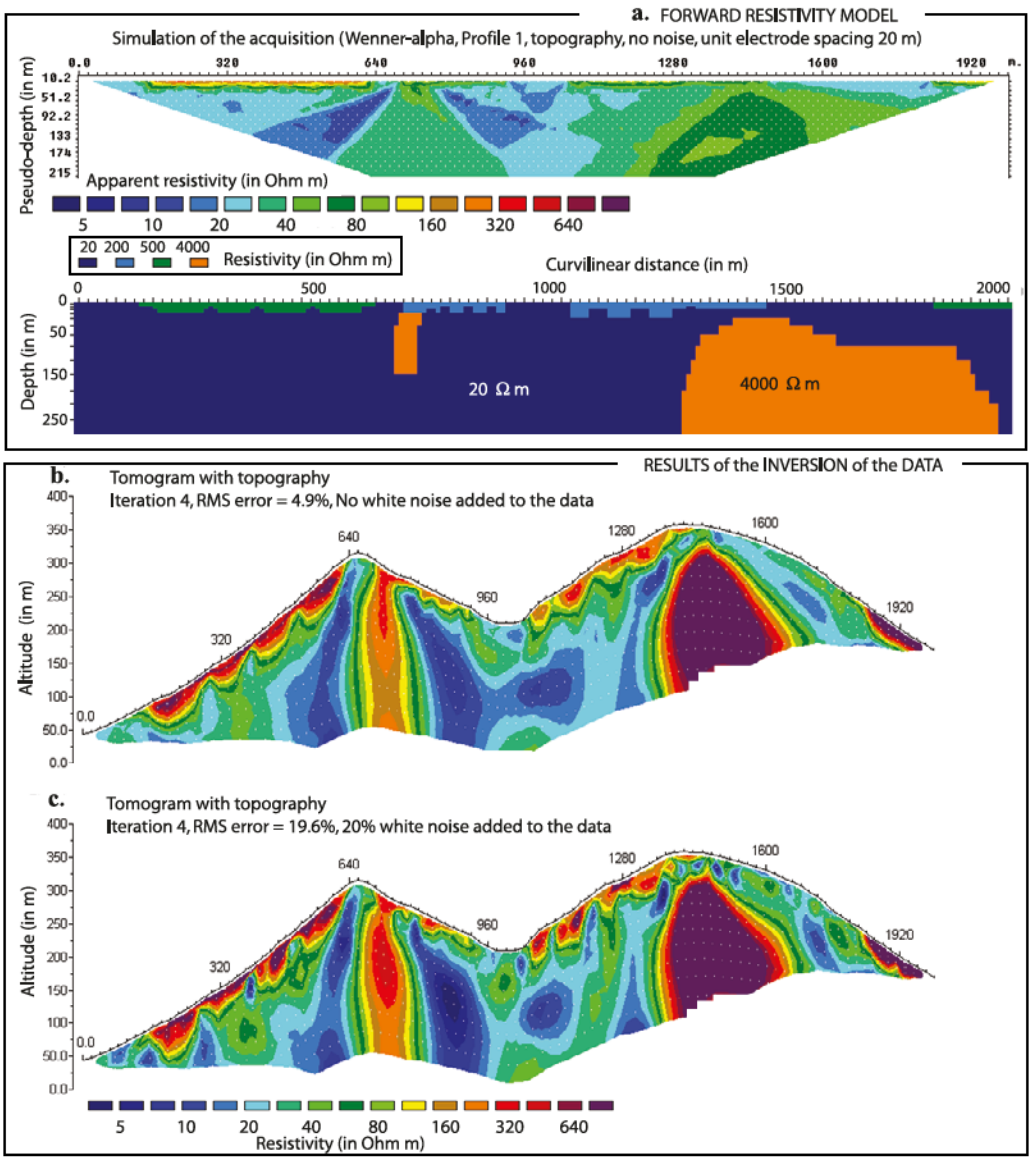

Figure 10. Sensitivity analysis of the resistivity data along profile 1. (a) We have used a simple resistivity structure by trial and error that can reproduce the resistivity data. In the example shown here we did not try to model the resistivity anomaly observed in the inversion of the data below the bottom of the crater (see Figure 11a). (b and c) The resistivity anomaly below of the bottom of the crater is not found, even with 20% of white noise added to the data. Therefore it seems that this structure is not an artifact. The high RMS error found with this profile (25% at the fourth iteration) seems to be the result of random noise existing in the data because of the low injected current.

the samples. Then the samples were dried at 60°C for 4 days and their weights measured. Finally, the samples were saturated with degassed water under vacuum and let stand for 2 additional days to allow complete saturation of the connected porosity. Weight measurements of the saturated samples were carried out after that time. The saturated samples were weighted in air and water (buoyancy weight). Values of the porosity are reported in Table 2. A correlation between the formation factors and the connected porosities (not shown here) indicates that the formation factor is related to the porosity by an Archie's law $F = \phi^{-m}$ with $m \approx 2.0 \pm 0.1$.

5. Interpretation and Discussion

5.1. Uncertainty Associated With the Resistivity Data

[33] The analysis of the uncertainty associated with the interpretation of the self-potential data in terms of groundwater flow will be discussed below in section 5.5. We discuss below the uncertainty associated with the resistivity data, which show large RMS error (up to 25% at the fourth iteration). We performed a sensitivity analysis using profile

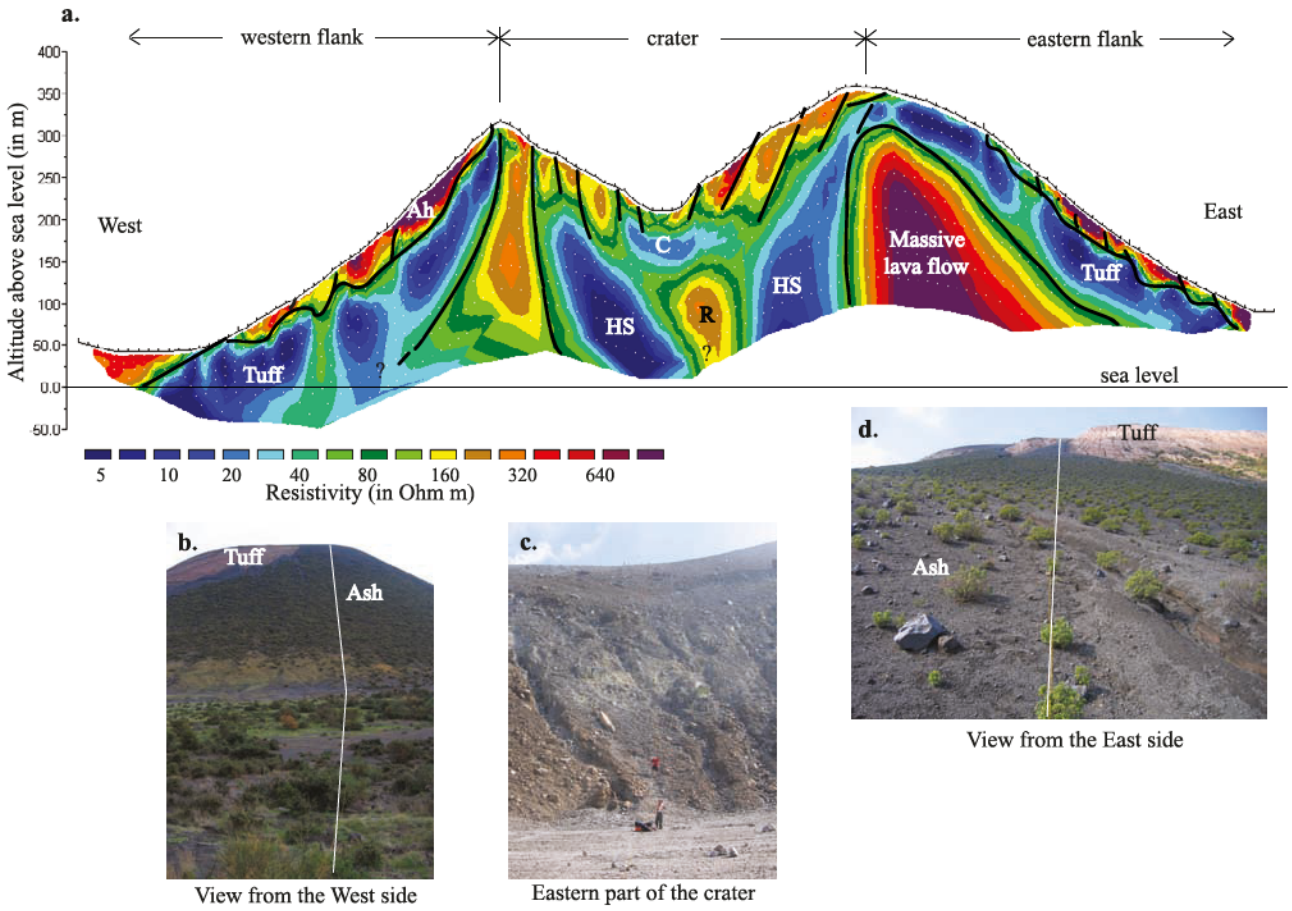

Figure 11. (a) Architecture of the Fossa cone along the profile 1 (resistivity tomogram). Abbreviations are as follows: Ah, ash; HS, hydrothermal system; C, conductive; and R, resistive. (b and d) Pictures of the Fossa cone from the west and east sides showing the position of the ashes relatively to the position of the hydromagmatic tuff (the line shows the position of the profile). (c) Picture taken inside the crater showing the pyroclastic deposits.

1. We were especially interested by this profile to see if the resistive structure found at depth below the bottom part of the crater (see Figure 11a) was an artifact or not.

[34] To perform the sensitivity analysis, we followed the following steps (1) We used a simple resistivity distribution for this profile (see Figure 10a); (2) we used the finite element code RESMOD to simulate the acquisition of the data using the resistivity distribution and the known topography; (3) we contaminated these synthetic data with various levels of (white) noise; (4) we run RES2DINV on these profiles to invert the synthetic apparent resistivity data; and (5) we compare the inverted results with the input resistivity data. The results are the following (see Figure 10): (1) the resistive structure below the bottom of the crater is probably not an artifact because it cannot be reproduced without the presence of a resistive body at this location; (2) the deep resistive body on the flanks of the volcanoes have a higher resistivity values than obtained from the resistivity tomograms (by using a trial and error approach, we obtained a resistivity value of 4000 ± 1000 Ω m); (3) the high RMS error is essentially due to the noise existing in the raw data because of the relatively low current injected in the ground. However, adding white noise to the data does not change the result of the inversion. It just changes the RMS value. Consequently, the inverse modeling is very robust to the presence of such a noise.

5.2. Flanks

[35] Along the east-west direction (see profile 1 for example), we observe a relatively simple architecture from the electrical resistivity tomogram. A resistive ash layer (100–1000 Ω m, 500 Ω m according to Figure 10) covers a conductive tuff layer (5 to 50 Ω m; see Figures 4 and 11). At depth, a highly and continuous resistive body is observed on both sides of the volcano (Figures 4 and 11). We interpret this body as corresponding to massive lava flow units with resistivity in the range 100 to 5000 Ω m (4000 Ω m according to Figure 10). No thermal anomalies are observed at the ground surface along the flanks. The self-potentials exhibit a classical W-shape [*Ishido*, 2004], which is traditionally interpreted as the effect of the upwelling of hydrothermal fluids in the central part of the edifice and the downward flow of meteoritic groundwater along the flanks of the edifice [*Michel and Zlotnicki*, 1998; *Revil et al.*, 2003]. This self-potential anomaly is quantitatively modeled in section 5.5.

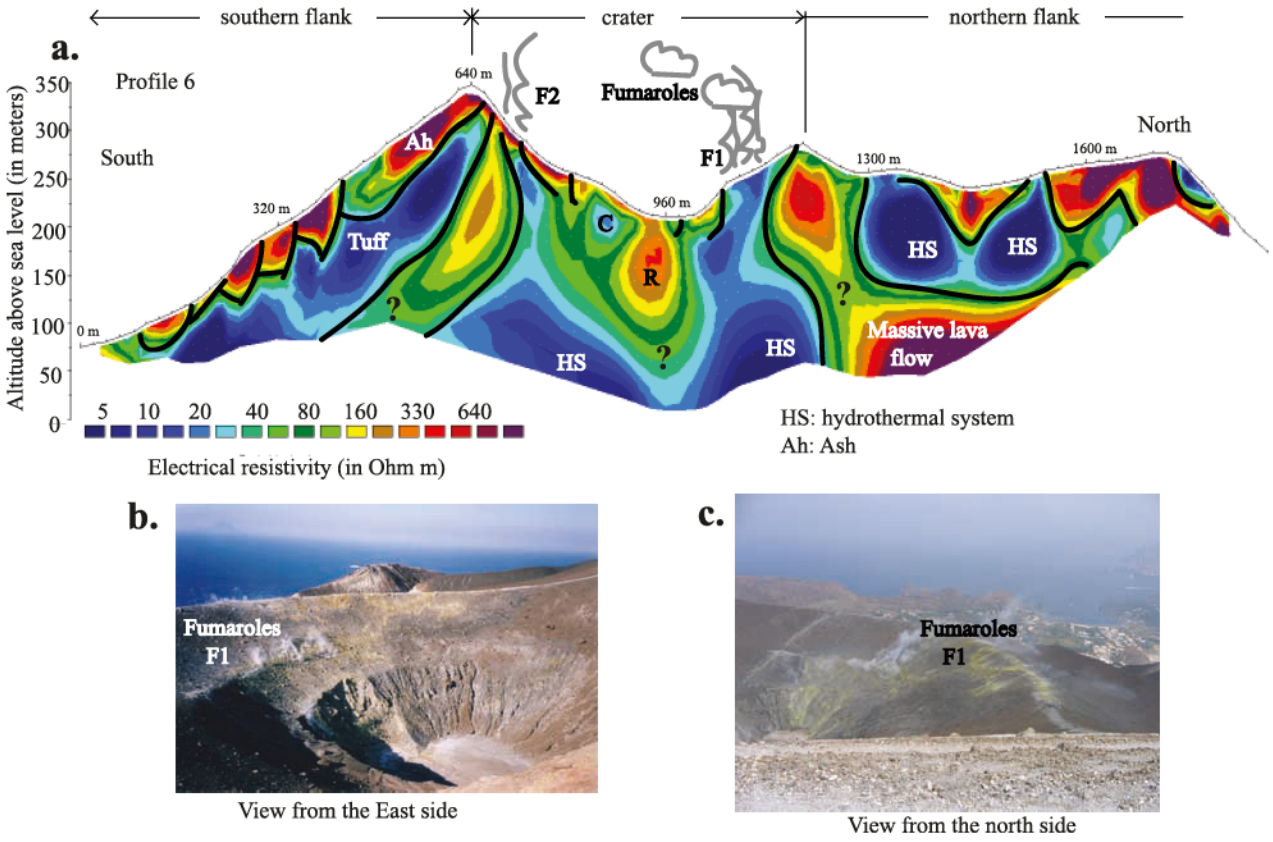

Figure 12. Architecture of the Fossa cone along the profile 6. The root of the area of fumarolic activity can be extended to a depth of 200 m below the ground surface. Abbreviations are as follows: F1 and F2, fumaroles; Ah, ash; HS, hydrothermal system. The internal part of the crater is characterized by a pocket of high conductivity (C) and a high resistivity structure (R).

[36] Profile 3 is nearly perpendicular to profile 1 (see Figure 5). This profile shows a very complex pattern by comparison with profile 1 and the existence of thermal anomalies. This complex pattern results from the evolution of the volcano over time (see Figure 5). It crosses in the northern part of the profile, temperature anomalies related to the crater boundaries of Forgia Vecchia. The first (and the most important) of the two Forgia Vecchia craters, Forgia Vecchia I, was formed during the 6th century B.C. [*Giacomelli and Scandone*, 2002]. The second crater, Forgia Vecchia II, was formed in 1727 A.D. [*Frazzetta and La Volpe*, 1991], just before the extrusion of the Pietre Cotte obsidian lava flow that occurred in 1739 A.D. [*De Fiore*, 1922].

5.3. Hydrothermal System

[37] Fumarolic activity indicates that the extension of the hydrothermal system is constrained by the boundary of the main crater, except for the area of Forgia Vecchia (see location Figure 1). The temperature map (Figure 8) shows that the main structural morphological crater boundaries, identified by previous geological mapping, serve as preferential fluid flow pathways for the upwelling of hot fluids. These structural boundaries are: (1) the southern crater rim of Caruggi cycles [*De Astis et al.*, 2007] representing the ex-Commenda cycle; (2) the Fossa I crater rim located in the eastern part of the edifices; (3) different imbricated crater boundaries constituting the present-day cone of Vulcano also called La Fossa cone or Gran Cratere (post-1739); and (4) a small temperature peak on Forgia Vecchia crater rim, in the northern part of the edifice. This shows that all the geological crater boundaries, constituting the actual cone of Vulcano, act as preferential flowpaths for heated hydrothermal fluids. The hydrothermal system is mainly contained inside the boundary of the craters including Forgia Vecchia. All the crater boundaries exhibit thermal anomalies (Figures 4–8). These boundaries are planes of mechanical weakness along which cracks are periodically reopened by tectonic activity of the volcano during crises affecting La Fossa di Vulcano [see *Granieri et al.*, 2006].

[38] We have no idea about the nature of the resistive body lying below the bottom part of the crater (Figure 11a). However, this body if not an artifact owing to the influence of the topography on the inversion of the resistivity data (see Figure 10). It could be either a low-porosity body (the neck of the old magmatic chamber) or dry steam in the hydrothermal system. A future study will monitor the resistivity and self-potential changes along a profile crossing the crater of La Fossa to see how stable is this anomaly and the positive self-potential anomaly observed in the crater.

[39] Figure 12 shows the architecture of the Fossa cone along a SW-NE profile. The area of the highest-temperature fumarolic activity (noted "F1" in Figure 12) can be extended to a depth of 200 m corresponding to a conductive

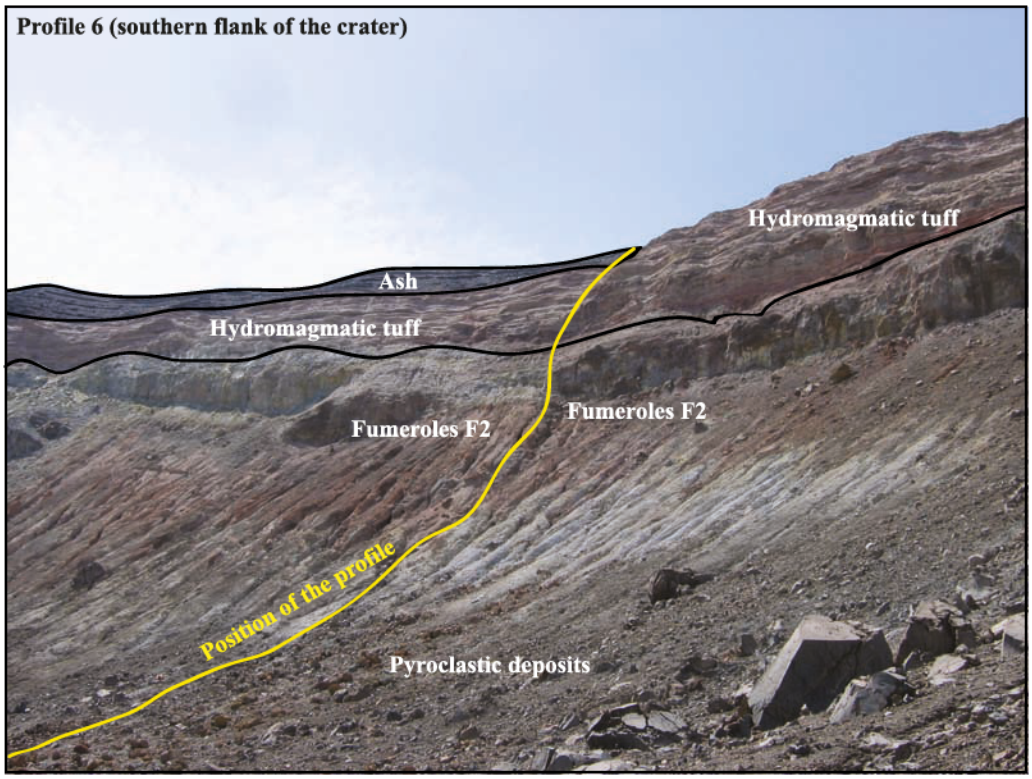

Figure 13. Architecture of the southern part of the crater along profile 6 with the position of the fumerole 2 (F2).

region. The high-conductivity region is probably related to the presence of alteration products (clays and zeolites) combined with the high temperatures inside this zone [see *Lénat et al.*, 2000; *Revil et al.*, 2003; *Bernard et al.*, 2007]. Figure 13 shows a picture of the southern part of the crater. All the structures observed at the ground surface can be observed on the resistivity tomogram (compare Figures 12 and 13).

[40] Below the sea level, high values of the conductivity are associated with the intrusion of the seawater. This can explain the disappearance of some of the structures below the sea level (e.g., on the right-hand side of profile 1; see Figure 4). Therefore, when interpreting resistivity profiles, we have to keep in mind that the relationship between resistivity and lithology is far from being unique.

5.4. Flow Pattern at Vulcano

[41] We use the finite element code Comsol Multiphysics 3.3 to determine the distribution of the streaming electrical potential associated with groundwater flow [see *Bolève et al.*, 2007b]. Such numerical simulations can be used to assess the geometry of groundwater flow of volcanoes and geothermal systems. The physics of these streaming potentials can be explained as follows: The existing charge at the surface of the minerals in contact with water is counterbalanced by an excess of electrical charges of opposite polarity located in the pore water. The flow of pore fluid drags the excess of electrical charge contained creating an electrical current density called the streaming current density.

[42] In this section, we use the resistivity profile measured along the east-west profile to simulate groundwater flow along this profile and to compute the resulting self-potential profile. Using the recent model developed by *Revil et al.* [2005] and *Revil and Linde* [2006], the total current density $\mathbf{j}$ (in A m^{-2}) is given by,

$$\mathbf{j} = \sigma \mathbf{E} + \bar{Q}_v \mathbf{u}, \tag{4}$$

where $\mathbf{u}$ is the Darcy's velocity (in m s^{-1}), $\mathbf{E} = -\nabla\varphi$ is the macroscopic electrical field (in V m^{-1}), φ is the electrical (self-) potential (in V), and $\bar{Q}_v$ is the excess of charge (of the diffuse layer) of the pore water per unit pore volume (in C m^{-3}). The streaming potential coupling coefficient defined by equation (3) and the excess of charge $\bar{Q}_v$ are related to each other and to the hydraulic conductivity K (in m s^{-1}) by $C = \partial\varphi/\partial H = -\bar{Q}_v K/\sigma$ where H is the hydraulic head [*Revil et al.*, 2005]. This formulation has been recently extended to unsaturated conditions by *Linde et al.* [2007] and *Revil et al.* [2007].

[43] According to equation (4), the distribution of the self-potential is sensitive to the pattern of the Darcy velocity $\mathbf{u}$. Therefore, the mechanism generating the flow itself (gravitational flow, free or forced convection) is rather unimportant regarding the distribution of the self-potential signals. We determine the flow pattern by using Darcy's law:

$$\mathbf{u} = -K\nabla H, \tag{5}$$

where $\Delta H = \delta p/\rho_f g$ is the change in hydraulic head (above or below the hydrostatic initial distribution H_0), δp is the excess of pressure above or below the hydrostatic level, ρ_f is

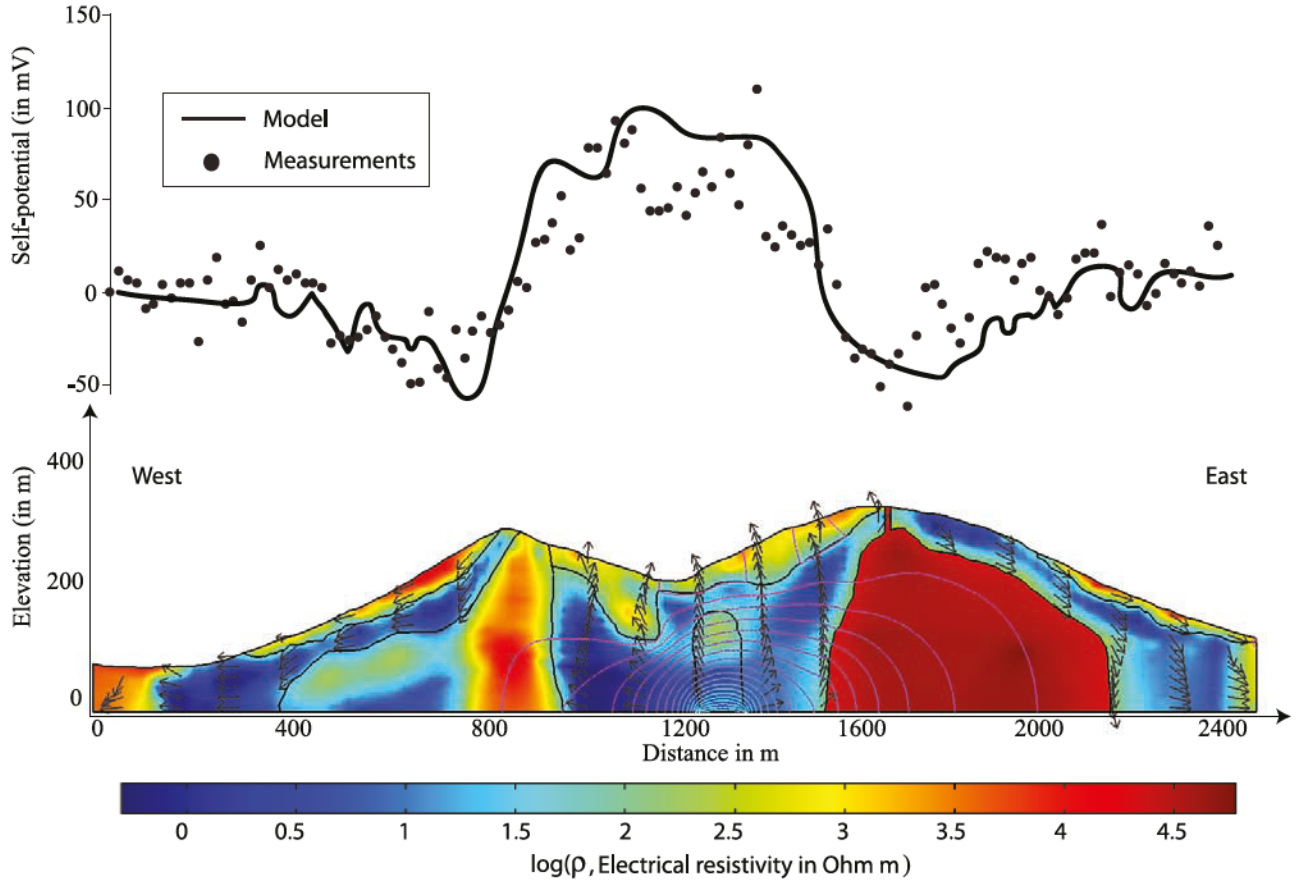

Figure 14. Finite element model of groundwater flow (the arrows represent the normalized seepage velocities) and resulting self-potential distribution at the ground surface of the Fossa cone obtained using a finite element code (Comsol Multiphysics 3.3). The negative self-potential anomaly along the flanks of the volcan results from the percolation of the groundwater in shallow aquifers while the positive self-potential anomaly inside the crater is due to the upflow of the hydrothermal fluids (profile 1).

the pore fluid density (in kg m^{-3}), and g is the acceleration of the gravity (in m s^{-2}). The Darcy's law is combined with the continuity equation for the mass of the pore fluid to give:

$$S\frac{\partial H}{\partial t} = \nabla \cdot (K\nabla H), \tag{6}$$

where t is time, s (in m^{-1}) is the poroelastic storage coefficient at saturation. The following computation is performed for steady state conditions and therefore the flow is given by solving $\nabla(K\nabla H) = 0$. The flow can be imposed by using appropriate boundary conditions and conservation of pore water flux. Here, we impose the flux at the boundaries of the system.

[44] The continuity equation, for the electrical charge is $\nabla \cdot \mathbf{j} = 0$. Combining this equation with equation (4) results in Poisson equation for the electrical potential with a source term that depends only on the seepage velocity in the ground:

$$\nabla \cdot (\sigma\nabla\varphi) = \Im, \tag{7}$$

where $\Im$ is the volumetric current source density (in A m^{-3}) given by,

$$\Im = \bar{Q}_v \nabla \cdot \mathbf{u} + \nabla\bar{Q}_v \cdot \mathbf{u}, \tag{8}$$

[45] The resistivity distribution determined along profile 1 (see Figure 4) was imported into the commercial finite element software Comsol Multiphysics 3.3. The resistivity cross section was discretized in several blocks (each block was then discretized using triangular meshing). The blocks represent the ash, tuff, inner massive lava flow units, and the hydrothermal system. In addition to the value of the resistivity, we need the values of the permeability and the streaming current coupling coefficient plus boundary conditions for the current density (or the electrical potential) and the hydraulic head (or the flux of water) to determine the groundwater flow under steady state conditions. We use $C = -5$ mV m^{-1} and $k = 10^{-10}$ m^2 for the ashes, $C = -3$ mV m^{-1} and $k = 10^{-14}$ m^2 for the tuff, $C = -5$ mV m^{-1} and $k = 10^{-11}$ m^2 for the hydrothermal system. We assign a zero permeability to the massive lava flow units; accordingly the coupling coefficient in this unit does not matter. We have also to

worry about the temperature dependence of the material properties because of the elevated field temperatures in the volcanic edifice. However, the resistivity data are taken directly from the ERT profiles so they include the effect of the temperature. *Revil et al.* [2002] have shown that the value of the streaming potential coupling coefficient of volcaniclastic rocks is independent of the temperature so we do not have to worry about the direct influence of the temperature upon the coupling coefficient used to perform the simulation in this study.

[46] The simulated groundwater flow pattern is shown on Figure 14. There is a downward flow inside the ashes and the tuff materials along the flanks of the volcano while there is an upward flow inside the boundary of the crater. As shown from the CO_2 data, there is no seal (very low permeability unit) inside the crater (except maybe at the bottom part of the crater). The upward flow of the hot pore water is responsible for pronounced evaporation of water inside the crater boundaries. To check if this pattern of groundwater flow is compatible with the self-potential data, we determine the resulting self-potential distribution along profile 1. The simulated self-potential profile agrees quite well with the measured self-potential profile (Figure 14). In turn, this means that we could invert the measured self-potential data to determine the distribution of the Darcy velocity of the water phase inside the edifice. This is performed in the next section.

5.5. Inversion of Self-Potential Data

[47] The self-potential data are governed by a Poisson equation with a source term given by the divergence of the source (streaming) current density. Inverting Poisson equations is a well-established problem in the interpretation of magnetic and gravity data. Recently, various algorithms have been proposed to invert self-potential data in terms of the divergence of the current density [*Minsley et al.*, 2007], the three components of the current density itself [*Jardani et al.*, 2007; *Linde and Revil*, 2007b], or the position of the source [*Jardani et al.*, 2006a].

[48] In this paper, we follow the methodology proposed recently by *Jardani et al.* [2007]. The relationship between the electrical current density and the measured SP signals can be written as,

$$\varphi(P) = \int_{\Omega} \mathbf{K}(P,M)\mathbf{j}_s(M)dV, \tag{9}$$

where $\mathbf{j}_s$ is the source current density (in both saturated and unsaturated conditions) described in section 2 and $\mathbf{K}(P,M)$ is the kernel connecting the SP data measured at a set of nonpolarizing electrodes P (with respect to a reference electrode) and the source of current at point M in the conducting ground of support Ω. The components of the kernel correspond to the Green's function of the problem. The kernel depends on the number of measurement stations at the ground surface, the number of discretized elements in which the source current density is going to be determined, and the resistivity distribution of the medium. The inversion of the SP data follows a two-step process. The first step is the inversion of the distribution of the current density $\mathbf{j}_s$. The second step is the determination of $\mathbf{u}$ using the distribution of $\mathbf{j}_s$ and assuming values for the excess charge density and, eventually, an a prior distribution of the current density determined by a prior model of groundwater flow.

[49] We propose to determine the current density by finding the minimum of the following objective function ψ,

$$\psi = (\mathbf{Km} - \varphi_d)^T \mathbf{W}_d (\mathbf{Km} - \varphi_d) + \lambda^2 (\mathbf{m} - \mathbf{m}_0)^T \mathbf{W}_k^m (\mathbf{m} - \mathbf{m}_0), \tag{10}$$

where λ is the regularization parameter ($0 < \lambda < \infty$; see *Tikhonov and Arsenin* [1977]), $\mathbf{K} = (\mathbf{K}_{ij}^x, \mathbf{K}_{ij}^z)$ is a Nx$2M$ matrix corresponding to the kernel, which can be measured by each component of a current density source $\mathbf{m} = (\mathbf{j}_i^x, \mathbf{j}_i^z)$, N is the number of self-potential stations and M is the number of discretized cells composing the ground, $2M$ represents the number of elementary current sources to consider (one horizontal component and one vertical component per cell for a 2-D problem), $\mathbf{m}$ is the vector of $2M$ model parameters (source current density), $\boldsymbol{m}_0$ is an a prior distribution of the source current density, $\mathbf{W}_d = \mathrm{diag}\{1/\varepsilon_{1,\ldots,1/\varepsilon_N}\}$ is a square diagonal weighting NxN matrix (elements along the diagonal of this matrix are the reciprocal of the standard deviation ε_i of the data), and φ_d is a vector of N elements corresponding to the self-potential measurements at the surface of the volcano. In our analysis, we took a mean deviation standard of 12 mV by analyzing the self-potential data along profile 1 (mean and standard deviation). The standard deviation is mainly due to heterogeneity in the resistivity distribution just around the self-potential measurement stations.

[50] The matrix $\mathbf{W}_k^m$ corresponds to a kth-order derivative. The first- and second-order derivative are given by,

$$\mathbf{W}_1^m = \begin{bmatrix} 1 & -1 & 0 & 0 & \ldots & 0 \\ 0 & 1 & -1 & 0 & \ldots & 0 \\ \vdots & & \ddots & \ddots & & \vdots \\ \vdots & & & \ddots & \ddots & \vdots \\ 0 & \ldots & 0 & 1 & -1 & 0 \\ 0 & \ldots & 0 & 0 & 1 & -1 \end{bmatrix}, \tag{11}$$

$$\mathbf{W}_2^m = \begin{bmatrix} 1 & -2 & 1 & 0 & \ldots & 0 \\ 0 & 1 & -2 & 1 & \ldots & 0 \\ \vdots & & \ddots & \ddots & & \vdots \\ \vdots & & & \ddots & \ddots & \vdots \\ 0 & \ldots & 1 & -2 & 1 & 0 \\ 0 & \ldots & 0 & 1 & -2 & 1 \end{bmatrix}. \tag{12}$$

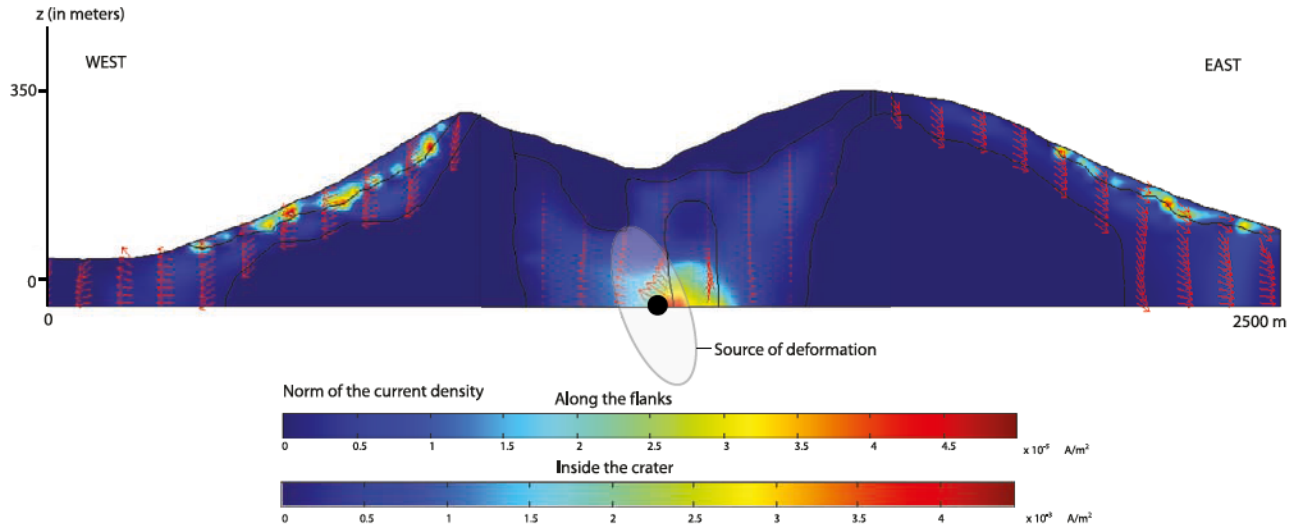

Figure 15. Determination of the sources of current density in the system associated with the flow of the groundwater. The ellipsoid corresponds to the deflation source volume observed by *Gambino and Guglielmino* [2008] for the period 1990–1996 inverting electro-optical and leveling measurements in an elastic homogeneous and isotropic half-space.

To account for the depth sensitivity of the source, we use a depth weighting diagonal matrix **S**. If the medium has a homogeneous resistivity distribution, it is defined from the depth weighting function:

$$\mathbf{S} = \begin{bmatrix} \frac{1}{(z_{m_1}+\varepsilon)^{\beta}} & 0 & \cdots & 0 \\ 0 & \frac{1}{(z_{m_2}+\varepsilon)^{\beta}} & \cdots & 0 \\ \vdots & \vdots & \ddots & \vdots \\ 0 & 0 & \cdots & \frac{1}{(z_{m_{2M}}+\varepsilon)^{\beta}} \end{bmatrix}, \quad (13)$$

where the small value ε is used to prevent the singularity when z is close to zero. The depth weighting (Nx3M) matrix is required to reduce the large sensitivity of the shallow cells [*Li and Oldenburg*, 1998; *Boulanger and Chouteau*, 2001; *Chasseriau and Chouteau*, 2003]. In the general case, the depth weighting is given by [e.g., *Spinelli*, 1999],

$$\mathbf{S} = \mathrm{diag}\left(\frac{1}{N}\sqrt{\sum_{j=1}^{N}(K_{ij})^2}\right). \quad (14)$$

[51] The solution of the problem is to find the unknown vector **m** corresponding to the minimum of the cost function given by $\partial\psi/\partial\mathbf{m} = 0$. This minimum is given by [*Hansen*, 1992]:

$$\mathbf{m}_w = \left[\mathbf{K}_w^T(\mathbf{W}_d^T\mathbf{W}_d)\mathbf{K}_w + \lambda(\mathbf{W}_m^T\mathbf{W}_m)\right]^{-1}\left[\mathbf{K}_w^T(\mathbf{W}_d^T\mathbf{W}_d)\varphi_d + \lambda(\mathbf{W}_m^T\mathbf{W}_m)\mathbf{m}_0\right]. \quad (15)$$

where $\mathbf{K}_w = \mathbf{K}\mathbf{S}^{-1}$ The model vector is finally then given by $\mathbf{m}^* = \mathbf{S}\mathbf{m}_w$. Because the model is linear with respect to the source current density, the solution, in terms of streaming current density, is obtained directly from equation (13). However, the solution of the inverse problem depends on the value of the regularization parameter and the value of the a prior model $\mathbf{m}_0$. To determine the value of the regularization parameter, *Hansen* [1998] proposed to plot the norm of the regularized smoothing solutions versus the norm of the residuals of the data misfit function. The resulting curve is hyperbolic and has therefore an L-shape. The determination of the regularization parameter, which is chosen at the corner of the L-shape plot, is known as the L-shape method. This is this method that we follow below.

[52] An alternative method is the cross-validation method [*Desbat and Girard*, 1995]. The cross-validation method allows choosing the best estimate of the regularization parameter in terms of the overall error prediction of the self-potential data. The total error prediction E(λ) is defined by,

$$\mathrm{E}(\lambda) = \frac{1}{N}\sum_{i=1}^{N}\left(\varphi_i^d - \varphi_i^*(\lambda)\right)^2, \quad (16)$$

where φ_i^d are the measured self-potential data and $\varphi^*_i(\lambda)$ are the estimate of the self-potential data at each self-potential station for a choice of the regularization parameter λ The best choice of the regularization parameter is obtain to reach the condition Min E(λ).

[53] The determine the resolution of the inverse problem, we can introduce the resolution matrix of the self-potential problem. The forward model is given by $\bar{\varphi} = \mathbf{K}\mathbf{m}$ where $\bar{\varphi}$ is the self-potential vector. The solution of the inverse problem is given by $\mathbf{m}^* = \mathbf{T}\bar{\varphi}$ where **T** is the inverse transformation matrix. The resolution matrix **R** is defined by $\mathbf{m}^* = \mathbf{R}\mathbf{m}$ with $\mathbf{R} = \mathbf{K}\mathbf{T}$ [*Menke*, 1989]. The resolution matrix contains all the information related to the uncertainty of the solution $\mathbf{m}^*$ for any cell of the investigated source volume.

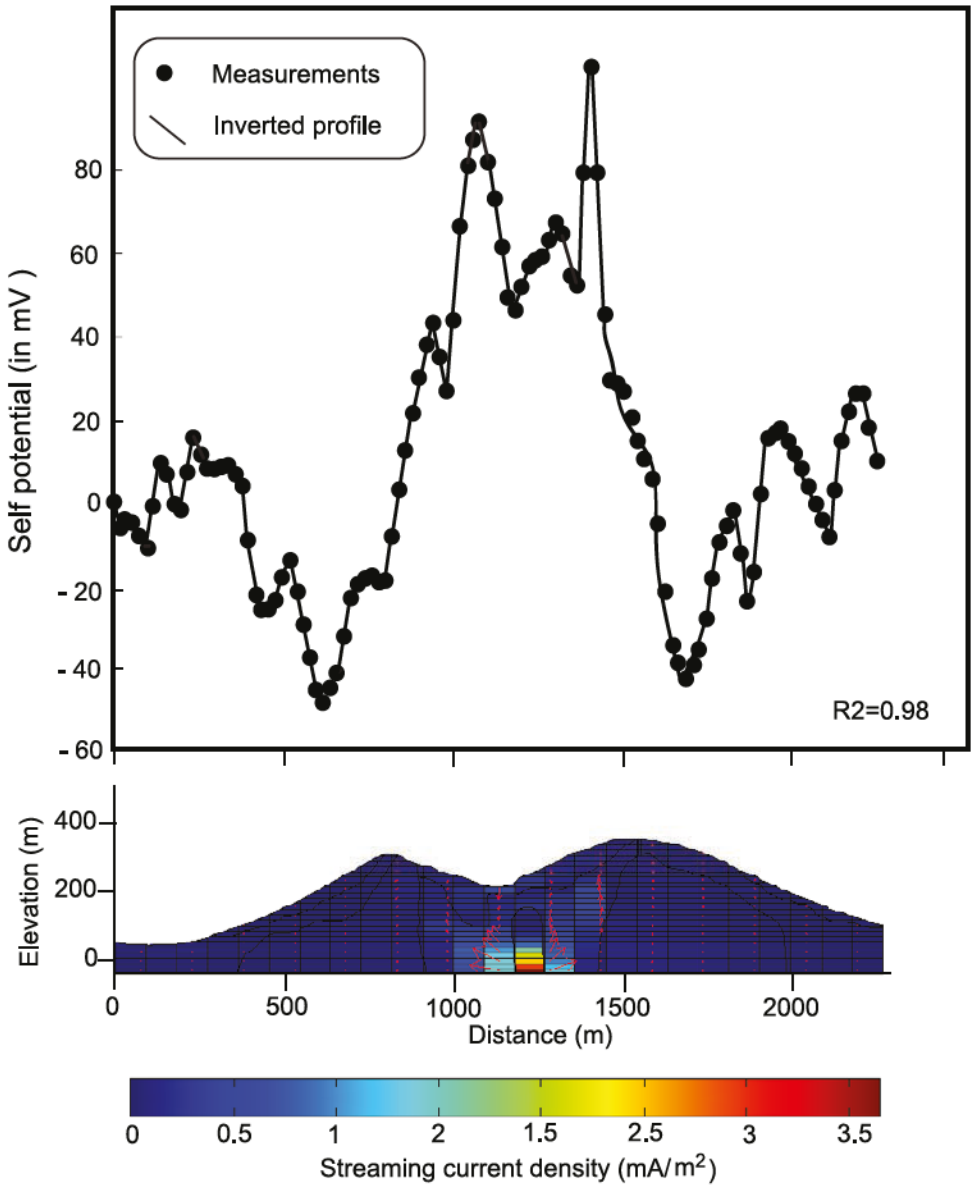

Figure 16. Inversion of the self-potential data in terms of the streaming current density. (a) Comparison between the measured self-potential data and the self-potential determined from the inverted model (R^2 = 0.98). (b) Result of the inversion of the self-potential data with a depth weighting matrix and a derivative operator of order one. The arrows represent the direction of the current density vector.

[54] The steps we follow to invert the self-potential data on profile 1 are the following:

[55] 1. We determine an a prior model of fluid flow using the geometrical structure inferred from the electrical resistivity tomogram along this profile, a prior permeability value that we believe to be reasonable for the four types of formations used to interpret the resistivity tomogram, and boundary conditions for the flow. The result is shown on Figure 14 and provides already a good fit of the self-potential data. Then we use this groundwater flow solution to determine $\boldsymbol{m}_0$, the a prior distribution of the source current density (Figure 15). This solution has not to be very precise but physically meaningful to place a prior constraints on the inversion of the self-potential data and to reduce the nonuniqueness of the solution.

[56] 2. The second step is the determination of the kernel. For each discretized cell, we consider a collection of M elementary source (in 2-D, there are $2M$ components of the current density to retrieve) and N observation stations P. When computing the elements of $\boldsymbol{K}$, one has to remember that the electrical potential is determined relatively to a reference electrode. In our case, the reference electrode is placed at the first station at the beginning of the profile). By definition, the electrical potential at the reference is taken as equal to zero and this condition should be fulfilled for all the elements of $\boldsymbol{K}$ by removing the potential computed at this location from the self-potential distribution determined over the field. By computing the kernel, we also take into account the ground topography. In computing the kernel, we can also to choose to restrain the solution to subvolumes of the volcanoes. In the present case, we consider that the very

resistive units are low-porosity units which can be consider as seals with a null permeability.

[57] 3. The third step is the determination of the regularization parameter using the L-shape method.

[58] 4. The final problem is the determination of the best fit solution using equation (15). The result of the inversion with the use if an a prior model is shown in Figure 16.

[59] We find that the source is mainly located below the crater (sources along the flanks are very minor; see Figure 16). Interestingly, the localization of the inverted source current density is consistent with the position of the source model inferred recently by *Gambino and Guglielmino* [2008] for the subsidence of the Fossa edifice that occurred during the period 1990–1996. During this period, electro-optical distance and leveling measurements were used by *Gambino and Guglielmino* [2008] to infer a shallow prolate ellipsoid responsible for the deformation of La Fossa Edifice. They explained the deformation as a transient migration of hydrothermal fluids along this source model. Because the current density evidences preferential fluid migration along a conduit, it is likely that deformation and self-potential data point out the same preferential fluid flow pathway below the crater of La Fossa volcano.

6. Conclusion

[60] The inner structure of La Fossa di Vulcano (Vulcano Island, southern Tyrrhenian Sea, Italy) is revealed by high-resolution electric resistivity tomography coupled with self-potential, temperature, and CO_2 gas flux measurements. These measurements provide an idea of the architecture of the edifice including the geometry of the ash, tuff, lava flow units, and the spatial organization of the hydrothermal system. Numerical modeling of the flow system along the east-west profile shows the downward percolation of water in the ash and tuff, and upward flow of groundwater inside the crater that is required to explain the observed self-potential data measured along this profile.

[61] Because of its relatively small size and importance in terms of geohazards, La Fossa di Vulcano is a very interesting natural laboratory to see how various geophysical methods can be integrated to reveal the architecture of a volcano and to monitor its thermohydromechanical behavior. In the near future, we plan to perform a three-dimensional joint inversion of electrical resistivity and gravity data. Such a joint inversion would probably be able to identify structural discontinuities of the edifice and to estimate both density and resistivity values for each subunit using a structural joint inversion approach [*Gallardo and Meju*, 2004] or sequential inversion approach with discrete values for the resistivity and the mass density [e.g., *Krahenbuhl and Li*, 2006]. The combination of various sources of information (passive seismic data, self-potential, ground deformation, and variation of the gravity field) is probably required to distinguish magmatic versus hydrothermal phenomena and their implications in the assessment of geohazards.

[62] **Acknowledgments.** The INSU-CNRS, Instituto di Metodologie per l'Analisi Ambientale del CNR, the Laboratoire GéoSciences Réunion-IPGP, the CNR, the Istituto Nazionale di Geofisica e Vulcanologia, and the Dipartimento per la Protezione Civile, through the DPC research program (V3.5 Vulcano, 2005–2007), are thanked for financial support. We also thank Xavier Rassion and Etienne Wheris for their help in the field, without forgetting Peppe Sansone for his inimitable Sicilian recipes. We thank also A. Jardani for his help and Maria Marsella for facilitating the use of Vulcano DEM. This is IPGP contribution 2294. We thank the associate editor, an anonymous referee, and David Fitterman for their very useful comments of our manuscript.

References

Aubert, M., S. Diliberto, A. Finizola, and Y. Chébli (2008), Double origin of hydrothermal convective flux variations in the Fossa of Vulcano (Italy), *Bull. Volcanol.*, doi:10.1007/s00445-007-0165-y, in press.

Auken, E., and A. V. Christiansen (2004), Layered and laterally constrained 2D inversion of resistivity data, *Geophysics*, *69*, 752–761.

Baldi, P., S. Bonvalot, P. Briole, M. Coltelli, K. Gwinner, M. Marsella, G. Puglisi, and D. Remy (2002), Validation and comparison of different techniques for the derivation of digital elevation models and volcanic monitoring (Vulcano Island, Italy), *Int. J. Remote Sens.*, *22*, 4783–4800.

Bedrosian, P. A., M. J. Unsworth, and M. J. S. Johnston (2007), Hydrothermal circulation at Mount St. Helens determined by self-potential measurements, *J. Volcan. Geotherm. Res.*, *160*, 137–146.

Bernard, M.-L., M. Zamora, Y. Géraud, and G. Boudon (2007), Transport properties of pyroclastic rocks from Montagne Pelée volcano (Martinique, Lesser Antilles), *J. Geophys. Res.*, *112*, B05205, doi:10.1029/2006JB004385.

Binley, A., and A. Kemna (2005), DC resistivity and induced polarization methods, in *Hydrogeophysics*, edited by Y. Rubin and S. Hubbard, chap. 5, pp. 129–156, Springer, New York.

Bolève, A., A. Crespy, A. Revil, F. Janod, and J. L. Mattiuzzo (2007a), Streaming potentials of granular media: Influence of the Dukhin and Reynolds numbers, *J. Geophys. Res.*, *112*, B08204, doi:10.1029/2006JB004673.

Bolève, A., A. Revil, F. Janod, J. L. Mattiuzzo, and A. Jardani (2007b), Forward modeling and validation of a new formulation to compute self-potential signals associated with ground water flow, *Hydrol. Earth Syst. Sci.*, *11*(5), 1661–1671.

Boulanger, O., and M. Chouteau (2001), Constraints in 3-D gravity inversion, *Geophys. Prospect.*, *49*, 265–280.

Chasseriau, P., and M. Chouteau (2003), 3D gravity inversion using a model of parameter covariance, *J. Appl. Geophys.*, *52*(1), 59–74.

Chiodini, G., F. Frondini, and B. Raco (1996), Diffuse emission of CO_2 from the Fossa crater, Vulcano Island (Italy), *Bull. Volcanol.*, *58*, 41–50.

Chiodini, G., R. Cioni, M. Guidi, L. Marini, and B. Raco (1998), Soil CO_2 flux measurements in volcanic and geothermal areas, *Appl. Geochem.*, *13*, 543–552.

Colella, A., V. Lapenna, and E. Rizzo (2004), High-resolution imaging of the High Agri Valley basin (southern Italy) with electrical resistivity tomography, *Tectonophysics*, *386*, 29–40.

Constable, S. C., R. L. Parker, and C. G. Constable (1987), Occam's inversion—A practical algorithm for generating smooth models from electromagnetic sounding data, *Geophysics*, *52*, 289–300.

Coppo, N., P.-A. Schnegg, W. Heise, P. Falco, and R. Costa (2008), Multiple caldera collapses inferred from the shallow electrical resistivity signature of the Las Cañadas caldera, Tenerife, Canary Islands, *J. Volcanol. Geotherm. Res.*, *170*, 153–166.

Cortecci, G., E. Dinelli, L. Bolognesi, T. Boschetti, and G. Ferrara (2001), Chemical and isotopic compositions of water and dissolved sulfate from shallow wells on Vulcano Island, Aeolian Archipelago, Italy, *Geothermics*, *30*, 69–91.

Corwin, R. F., and D. B. Hoover (1979), The self-potential method in geothermal exploration, *Geophysics*, *44*, 226–245.

De Astis, G., P. Dellino, L. La Volpe, F. Lucchi, and C. A. Tranne (2007), *Geological Map of the Vulcano Island*, scale 1:10000, edited by L. La Volpe and G. De Astis, Ist. Nat. Geofis. Vulcanol., Napoli, Italy.

De Fino, M., L. La Volpe, and G. Piccarreta (1991), Role of magma mixing during recent activity of La Fossa di Vulcano (Aeolian Islands, Italy), *J. Volcanol. Geotherm. Res.*, *48*, 385–398.

De Fiore, O. (1922), *Vulcano (Isole Eolie), Riv. Vulcanol.*, suppl. III, 393 pp., Fridlander Inst., Napoli, Italy.

Dellino, P., and L. La Volpe (1997), Stratigrafia, dinamiche eruttive e deposizionali, scenario eruttivo e valutazioni di pericolosità a La Fossa di Vulcano in *CNR-GNV Progetto Vulcano 1993–1995*, edited by L. La Volpe et al., pp. 214–237, Felici Publ., Pisa, Italy.

De Rosa, R., N. Calanchi, P. F. Dellino, L. Francalanci, F. Lucchi, M. Rosi, P. L. Rossi, and C. A. Tranne (2004), *32nd International Geological Congress, Field Trip Guide Book–P42, vol. 5, Geology and Volcanism of Stromboli, Lipari, and Vulcano (Aeolian Islands)*, edited by L. Guerrieri, I. Rischia, and L. Serva, Agency for the Environ. Prot. and Tech. Serv., Rome.

Desbat, L., and D. Girard (1995), The minimum reconstruction error choice of regularization parameters: Some more efficient methods and their

application to deconvolution problems, *SIAM J. Sci. Comput.*, *16*(6), 1387–1403.
Diaferia, I., M. Barchi, M. Loddo, D. Schiavone, and A. Siniscalchi (2006), Detailed imaging of tectonic structures by multiscale Earth resistivity tomographies: The Colfiorito normal faults (central Italy), *Geophys. Res. Lett.*, *33*, L09305, doi:10.1029/2006GL025828.
Di Fiore, B., P. Mauriello, and D. Patella (2004), On the localisation of long-standing self-potential sources at Vulcano (Italy) by probability tomography, *Quadernidi Geofis.*, *35*, 27–32.
Ellam, R. M., C. J. Hawkesworth, M. A. Menzies, and N. W. Rotgers (1989), The volcanism of southern Italy: Role of subduction and the relationship between potassic and sodic alkaline magmatism, *J. Geophys. Res.*, *94*, 4589–4601.
Finizola, A., S. Sortino, J.-F. Lénat, and M. Valenza (2002), Fluid circulation at Stromboli volcano (Aeolian Islands, Italy) from self-potential and CO2 surveys, *J. Volcanol. Geotherm. Res.*, *116*, 1–18.
Finizola, A., S. Sortino, J.-F. Lénat, M. Aubert, M. Ripepe, and M. Valenza (2003), The summit hydrothermal system of Stromboli. New insights from self-potential, temperature, CO2 and fumarolic fluid measurements, Structural and monitoring implications, *Bull. Volcanol.*, *65*, 486–504, doi:10.1007/s00445-003-0276-z.
Finizola, A., A. Revil, E. Rizzo, S. Piscitelli, T. Ricci, J. Morin, B. Angeletti, L. Mocochain, and F. Sortino (2006), Hydrogeological insights at Stromboli volcano (Italy) from geoelectrical, temperature, and CO_2 soil degassing investigations, *Geophys. Res. Lett.*, *33*, L17304, doi:10.1029/2006GL026842.
Fitterman, D. V., W. D. Stanley, and R. J. Bisdorf (1988), Electrical structure of Newberry volcano, Oregon, *J. Geophys. Res.*, *93*, 10,119–110,134.
Frazzetta, G., and L. La Volpe (1991), Volcanic history and maximum expected eruption at "La Fossa di Vulcano" (Aeolian Islands, Italy), *Acta Volcanol.*, *1*, 107–113.
Frazzetta, G., L. La Volpe, and M. F. Sheridan (1983), Evolution of the Fossa cone, Volcano, *J. Volcanol. Geotherm. Res.*, *17*, 329–360.
Frazzetta, G., P. Y. Gillot, L. La Volpe, and M. F. Sheridan (1984), Volcanic hazards at Fossa of Volcano: Data from the last 6,000 years, *Bull. Volcanol.*, *47*, 105–125.
Gallardo, L. A., and M. A. Meju (2004), Joint two-dimensional DC resistivity and seismic travel time inversion with cross-gradients constraints, *J. Geophys. Res.*, *109*, B03311, doi:10.1029/2003JB002716.
Gambino, S., and F. Guglielmino (2008), Ground deformation induced by geothermal processes: A model for La Fossa crater (Vulcano Island, Italy), *J. Geophys. Res.*, doi:10.1029/2007JB005016, in press.
Gasparini, C., G. Iannaccone, and R. Scarpa (1982), Seismotectonics of the Calabrian Arc, *Tectonophysics*, *84*, 267–286.
Gex, P. (1992), Geophysical survey in the region of the crater of Vulcano, Italy (in French), *Bull. Soc. Vaudoise Sci. Nat.*, *82*(2), 157–172.
Giacomelli, L., and R. Scandone (2002), *Vulcani e eruzioni, Pitagora Editrice, Boll. Della Soc. Geogr. Ital.*, vol. IX, pp. 478–480, La Soc. Geogr. Ital., Bologna, Italy.
Granieri, D., M. L. Carapezza, G. Chiodini, R. Avino, S. Caliro, M. Ranaldi, T. Ricci, and L. Tarchini (2006), Correlated increase in CO_2 fumarolic content and diffuse emission from La Fossa crater (Vulcano, Italy): Evidence of volcanic unrest or increasing gas release from a stationary deep magma body?, *Geophys. Res. Lett.*, *33*, L13316, doi:10.1029/2006GL026460.
Hansen, P. C. (1992), Analysis of discrete ill-posed problems by means of the L-curve, *SIAM Rev.*, *34*(4), 561–580.
Hansen, P. C. (1998), *Rank-Deficient and Discrete Ill-Posed Problems: Numerical Aspects of Linear Inversion*, 247 pp., SIAM, Philadelphia, Pa.
Hase, H., T. Hashimoto, S. Sakanaka, W. Kanda, and Y. Tanaka (2005), Hydrothermal system beneath Aso volcano as inferred from self-potential mapping and resistivity structure, *J. Volcanol. Geotherm. Res.*, *143*, 259–277.
Ishido, T. (2004), Electrokinetic mechanism for the "W" -shaped self-potential profile on volcanoes, *Geophys. Res. Lett.*, *31*, L15616, doi:10.1029/2004GL020409.
Ishido, T., T. Kiruchi, N. Matsushima, Y. Yano, S. Nakao, M. Sugihara, T. Tosha, S. Takakura, and Y. Ogawa (1997), Repeated self-potential profiling of Izu-Oshima Volcano, Japan, *J. Geomagn. Geoelectr.*, *49*, 1267–1278.
Jardani, A., A. Revil, F. Akoa, M. Schmutz, N. Florsch, and J. P. Dupont (2006a), Least squares inversion of self-potential (SP) data and application to the shallow flow of ground water in sinkholes, *Geophys. Res. Lett.*, *33*, L19306, doi:10.1029/2006GL027458.
Jardani, A., J. P. Dupont, and A. Revil (2006b), Self-potential signals associated with preferential groundwater flow pathways in sinkholes, *J. Geophys. Res.*, *111*, B09204, doi:10.1029/2005JB004231.
Jardani, A., A. Revil, A. Bolève, A. Crespy, J.-P. Dupont, W. Barrash, and B. Malama (2007), Tomography of the Darcy velocity from self-potential measurements, *Geophys. Res. Lett.*, *34*, L24403, doi:10.1029/2007GL031907.
Jin, G., C. Torres-Verdin, S. Devarajan, E. Toumelin, and E. C. Thomas (2007), Pore-scale analysis of the Waxman-Smits shaly-sand conductivity model, *Petrophysics*, *48*(2), 104–120.
Kalscheuer, T., M. Commer, S. L. Helwig, A. Hördt, and B. Tezkan (2007), Electromagnetic evidence for an ancient avalanche caldera rim on the south flank of Mount Merapi, Indonesia, *J. Volcanol. Geotherm. Res.*, *162*, 81–97.
Keller, J. (1980), The island of Vulcano, *Soc. Ital. Min. Petr.*, *36*, 368–413.
Krahenbuhl, R. A., and Y. Li (2006), Inversion of gravity data using a binary formulation, *Geophys. J. Int.*, *167*, 543–556.
Kulessa, B., B. Hubbard, and G. H. Brown (2003a), Cross-coupled flow modeling of coincident streaming and electrochemical potentials and application to subglacial self-potential data, *J. Geophys. Res.*, *108*(B8), 2381, doi:10.1029/2001JB001167.
Kulessa, B., B. Hubbard, G. H. Brown, and J. Becker (2003b), Earth tide forcing of glacier drainage, *Geophys. Res. Lett.*, *30*(1), 1011, doi:10.1029/2002GL015303.
Lénat, J. F. (2007), Retrieving self-potential anomalies in a complex volcanic environment: An SP/elevation gradient approach, *Near Surface Geophys.*, *5*(3), 161–170.
Lénat, J. F., D. Fitterman, D. B. Jackson, and P. Labazuy (2000), Geoelectrical structure of the central zone of Piton de la Fournaise volcano (Reunion), *Bull. Volcanol.*, *62*, 75–89.
Leroy, P., and A. Revil (2004), A triple layer model of the surface electrochemical properties of clay minerals, *J. Colloid Interface Sci.*, *270*, 371–380.
Li, Y., and D. W. Oldenburg (1998), 3-D inversion of gravity data, *Geophysics*, *63*, 109–119.
Linde, N., and A. Revil (2007a), Comment on "Electrical tomography of La Soufrière of Guadeloupe Volcano: Field experiments, 1D inversion and qualitative interpretation", by F. Nicollin et al., *Earth Planet Sci. Lett.*, *258*, 619–622, doi:10.1016/j.epsl.2006.02.020.
Linde, N., and A. Revil (2007b), Inverting self-potential data for redox potentials of contaminant plumes, *Geophys. Res. Lett.*, *34*, L14302, doi:10.1029/2007GL030084.
Linde, N., A. Revil, A. Bolève, C. Dagès, J. Castermant, B. Suski, and M. Voltz (2007), Estimation of the water table throughout a catchment using self-potential and piezometric data in a Bayesian framework, *J. Hydrol.*, *334*, 88–98.
Lo Cascio, P., and E. Navarra (1997), *Guida Naturalistica Alle Isole Eolie*, 112 pp., L'EPOS Publ., Palermo, Italy.
Loke, M. H., and R. D. Barker (1996), Rapid least-squares inversion of apparent resistivity pseudosections by a quasi-Newton method, *Geophys. Prospect.*, *44*, 131–152.
Maineult, A., Y. Bernabé, and P. Ackerer (2005), Detection of advected concentration and pH fronts from self-potential measurements, *J. Geophys. Res.*, *110*, B11205, doi:10.1029/2005JB003824.
Maineult, A., Y. Bernabé, and P. Ackerer (2006), Detection of advected, reacting redox fronts from self-potential measurements, *J. Contam. Hydrol.*, *86*, 32–52.
Massenet, F., and V. N. Pham (1985), Experimental and theoretical basis of self-potential phenomena in volcanic areas with reference to results obtained on Mount Etna (Sicily), *Earth Planet. Sci. Lett.*, *73*, 415–429.
Menke, W. (1989), *Geophysical Data Analysis: Discrete Inverse Theory, Int. Geophys. Ser.*, vol. 45, 289 pp., Academic Press, London.
Michel, S., and J. Zlotnicki (1998), Self-potential and magnetic surveying of La Fournaise volcano (Réunion island): Correlations with faulting, fluid circulation, and eruption, *J. Geophys. Res.*, *103*, 17,845–17,857.
Minsley, B. J., J. Sogade, and F. D. Morgan (2007), Three-dimensional source inversion of self-potential data, *J. Geophys. Res.*, *112*, B02202, doi:10.1029/2006JB004262.
Niwas, S., P. K. Gupta, and O. A. L. de Lima (2007), Nonlinear Electrical Conductivity Response of Shaly-Sand Reservoir, *Curr. Sci.*, *92*(5), 612–617.
Perrier, F., M. Trique, B. Lorne, J. P. Avouac, S. Hautot, and P. Tarits (1998), Electrical potential variations associated with yearly lake level variations, *Geophys. Res. Lett.*, *25*, 1955–1959.
Revil, A. (1995), Conductivité electrique et potentiel spontané dans les mileux poreux: De la theorie a l'analyse des mesures en forage, Ph.D. thesis, Univ. Louis Pasteur, Strasbourg, France.
Revil, A., and P. W. J. Glover (1998), Nature of surface electrical conductivity in natural sands, sandstones, and clays, *Geophys. Res. Lett.*, *25*, 691–694.
Revil, A., and N. Linde (2006), Chemico-electromechanical coupling in microporous media, *J. Colloid Interface Sci.*, *302*, 682–694.

Revil, A., L. M. Cathles, S. Losh, and J. A. Nunn (1998), Electrical conductivity in shaly sands with geophysical applications, *J. Geophys. Res.*, *103*, 23,925–23,936.

Revil, A., D. Hermitte, E. Spangenberg, and J. J. Cochemé (2002), Electrical properties of zeolitized volcaniclastic materials, *J. Geophys. Res.*, *107*(B8), 2168, doi:10.1029/2001JB000599.

Revil, A., G. Saracco, and P. Labazuy (2003), The volcano-electric effect, *J. Geophys. Res.*, *108*(B5), 2251, doi:10.1029/2002JB001835.

Revil, A., V. Naudet, and J. D. Meunier (2004a), The hydroelectric problem of porous rocks: Inversion of the water table from self-potential data, *Geophys. J. Int.*, *159*, 435–444.

Revil, A., A. Finizola, F. Sortino, and M. Ripepe (2004b), Geophysical investigations at Stromboli volcano, Italy. Implications for ground water flow, *Geophys. J. Int.*, *157*, 426–440.

Revil, A., P. Leroy, and K. Titov (2005), Characterization of transport properties of argillaceous sediments: Application to the Callovo-Oxfordian argillite, *J. Geophys. Res.*, *110*, B06202, doi:10.1029/2004JB003442.

Revil, A., N. Linde, A. Cerepi, D. Jougnot, S. Matthäi, and S. Finsterle (2007), Electrokinetic coupling in unsaturated porous media, *J. Colloid Interface Sci.*, *313*, 315–327, doi:10.1016/j.jcis.2007.03.037.

Rizzo, E., B. Suski, A. Revil, S. Straface, and S. Troisi (2004), Self-potential signals associated with pumping tests experiments, *J. Geophys. Res.*, *109*, B10203, doi:10.1029/2004JB003049.

Roberts, J. J., and W. Lin (1997), Electrical properties of partially saturated Topopah Spring tuff: Water distribution as a function of saturation, *Water Resour. Res.*, *33*, 577–587.

Santacroce, R., R. Cristofolini, L. La Volpe, G. Orsi, and M. Rosi (2003), Italian active volcanoes, *Episodes*, *26*(3), 227–234.

Shevnin, V., A. Mousatov, A. Ryjov, and O. Delgado-Rodriquez (2007), Estimation of clay content in soil based on resistivity modelling and laboratory measurements, *Geophys. Prospect.*, *55*, 265–275.

Spinelli, L. (1999), Analyse Spatiale de l'Activité Electrique Cérébrale: Nouveaux Développements (in French), Ph.D. thesis, 136 pp., Univ. Joseph Fourier-Grenoble I, Grenoble, France.

Storz, H., W. Storz, and F. Javobs (2000), Electrical resistivity tomography to investigate geological structures of the earth's upper crust, *Geophys. Prospect.*, *48*, 455–471.

Suski, B., E. Rizzo, and A. Revil (2004), A sandbox experiment of self-potential signals associated with a pumping-test, *Vadose Zone J.*, *3*, 1193–1199.

Suski, B., A. Revil, K. Titov, P. Konosavsky, M. Voltz, C. Dagès, and O. Huttel (2006), Monitoring of an infiltration experiment using the self-potential method, *Water Resour. Res.*, *42*, W08418, doi:10.1029/2005WR004840.

Tabbagh, A., and P. Cosenza (2007), Effect of microstructure on the electrical conductivity of clay-rich systems, *Phys. Chem. Earth*, *32*(1–7), 154–160.

Tikhonov, A. N., and V. Y. Arsenin (1977), *Solutions of Ill-Posed Problems*, John Wiley, New York.

Titov, K., A. Revil, P. Konasovsky, S. Straface, and S. Troisi (2005), Numerical modeling of self-potential signals associated with a pumping test experiment, *Geophys. J. Int.*, *162*, 641–650.

Tosha, T., N. Matsushima, and T. Ishido (2003), Zeta potential measured for an intact granite sample at temperatures to 200°C, *Geophys. Res. Lett.*, *30*(6), 1295, doi:10.1029/2002GL016608.

Waxman, M. H., and L. J. M. Smits (1968), Electrical conduction in oil-bearing sands, *Soc. Pet. Eng. J.*, *8*, 107–122.

Wishart, D. N., L. D. Slater, and A. E. Gates (2006), Self potential improves characterization of hydraulically-active fractures from azimuthal geoelectrical measurements, *Geophys. Res. Lett.*, *33*, L17314, doi:10.1029/2006GL027092.

Zohdy, A. A. R., and R. J. Bisdorf (1990), Schlumberger soundings near Medicine Lake, California, *Geophysics*, *55*, 956–964.

B. Angeletti and A. Crespy, Université Aix Marseille III, CNRS, Domaine de l'Arbois, F-13100 Aix en Provence, France.

M. Balasco, A. Perrone, S. Piscitelli, and E. Rizzo, Laboratory of Geophysics, IMAA, National Research Council, Cda S. Loja, Tito Scalo, PZ I-85050, Italy.

S. Barde Cabusson and S. Byrdina, Laboratoire Magma et Volcan, UMR6524, Université Blaise Pascal, IRD, CNRS, 34 avenue Carnot, F-63000 Clermont-Ferrand, France.

L. Bennati, Department of Earth and Atmospheric Sciences, Purdue University, 550 Stadium Mall Drive, West Lafayette, IN 47906, USA.

A. Bolève, Bâtiment Le Chablais, Domaine Universitaire, UMR5559, Equipe Volcan, Université de Savoie, INSU, LGIT, CNRS, F-73376 Le Bourget-du-Lac CEDEX, France.

N. Carzaniga, Department of Geology and Geosciences, Università Milano-Bicocca, Piazza della Scienza 4, I-20126 Milano, Italy.

F. Di Gangi, Istituto Nazionale di Geofisica e Vulcanologia, Sezione di Palermo, Via Ugo la Malfa 153, I-90146, Palermo, Italy.

A. Finizola and J. Morin, Laboratoire GéoSciences Réunion, UMR7154, UR, IPGP, 15 avenue René Cassin, BP 7151, F-97715, Saint Denis CEDEX 9, La Réunion, France.

A. Revil, Department of Geophysics, Colorado School of Mines, 1500 Illinois Street, Golden, CO 80401, USA. (arevil@mines.edu)

T. Ricci, INGV, Università Roma Tre, Sezione Roma 1, Via della Vasca Navale 79, I-00146, Roma, Italy.

M. Rossi, IPGP, CNRS, Place Jussieu, F-75252 Paris CEDEX 05, France.

E. Roulleau, GEOTOP-UQAM-McGill, Université du Québec, CP 8888 Montréal, QC, H3C 3P8, Canada.

B. Suski, Institut de Géophysique, Collège Propédeutique, Université de Lausanne, CH-1015 Lausanne, Switzerland.